Formulation and sequential numerical algorithms of coupled fluid/heat flow and geomechanics for multiple porosity materials

J. Kim *, E. Sonnenthal, and J. Rutqvist

Earth Sciences Division, Lawrence Berkeley National Laboratory. 1 Cyclotron Road 90R1116, Berkeley, CA 94720, USA

SUMMARY

We generalized constitutive relations of coupled flow and geomechanics for the isothermal elastic double porosity model in the previous study to those for the non-isothermal elastic/elastoplastic multiple porosity model, finding coupling coefficients and constraints of the multiple porosity model, and determining the upscaled elastic/elastoplastic moduli as well as relations between the local strains of all materials within a gridblock and the global strain of the gridblock. Furthermore, the coupling equations and relations between local and global variables provide well-posed problems, implying that they honor the dissipative mechanism of coupled flow and geomechanics. For numerical implementation, we modified the fixed-stress sequential method for the multiple porosity model. From the a priori stability estimate, the sequential method provides numerical stability when an implicit time stepping algorithm is used. This sequential scheme can easily be implemented by using a modified porosity function and its porosity correction.
In numerical examples, we observe clear differences among the single, double, and multiple porosity systems, and the multiple porosity model can reflect high heterogeneity that exists within a gridblock. We also identify considerably complicated physics in coupled flow and geomechanics of the multiple porosity systems, which cannot accurately be detected in the uncoupled flow simulation.

KEY WORDS: double porosity, multiple porosity, poromechanics, multiple interacting continua (MINC), fractured reservoirs, fixed-stress split

1. INTRODUCTION

Coupled fluid, heat, and mechanical processes are important in many engineering fileds. In mechanical engineering, coupled heat and mechanics (e.g., thermoelasticity, thermoplasticity) are considered to analyze interactions between deformation of a material body and thermal stress [1, 2]. Rapid movement of the body such as vibration can be a source in heat flow, and heat induces additional stress in mechanics, which can expand the body. In turn, the expanded body affects accumulation in heat flow because of the change in material volume. Coupled fluid, heat, and mechanical processes are also critically important in geo-engineering [3]. In geotechnical engineering, an increase (or decrease) of pore pressure causes dilation (or shrinkage) of porous media, which changes strain and stress fields [4, 5, 6, 7, 8]. These changes also affect pore-volume, resulting in variation of pore-pressure, again. In petroleum engineering, changes in permeability as well as porosity induced by geomechanics are critical issues in order to predict fluid flow and production accurately, for example, in hydraulic fracturing, reservoir compaction, and gas-hydrate recovery [9, 10, 11, 12, 13, 14]. In geological carbon storage, the effect of large scale injection

*Correspondence to: J. Kim, Earth Sciences Division, Lawrence Berkeley National Laboratory. 1 Cyclotron Road 90R1116, Berkeley, CA 94720, USA. Email: JihoonKim@lbl.gov

and pressure changes and associated potential for inducing earthquakes is a key technical issue that needs to be addressed [15]. The effect of temperature is important in applications involving substantial temperature changes, such as in nuclear waste disposal and geothermal energy extraction [16, 17]. Especially, in geothermal engineering, rigorous modeling of coupling between fluid, heat, and geomechanics, named thermoporomechanics, for fractured porous media is necessary, because those physics are highly nonlinear and closely interacted with each other.

Significant efforts have been made to find an appropriate modeling of thermoporomechanics. The theory of poroelasticity was developed for single porosity concept [18, 19, 20], and several authors have extended Biot's theory to generally coupled fluid, heat, and geomechanics, proposing slightly different constitutive relations and the corresponding experimental settings [21, 22, 23, 24]. These studies are directly applicable to coupled problems with the single porosity concept. However, in large fractured or composite porous media, the theory of single porosity has significant limitation not only in coupled flow and geomechanics [25, 26, 27] but also in flow-only simulations [28]. In particular, in coupled flow and geomechanics problems, [26] concluded that neglecting the importance of the fracture deformation may cause substantial errors in the fractured rock media, where the fracture and rock matrix coexist. To solve this problem, a double porosity concept (or its generalization such as multiple interacting continua method (MINC)) was proposed for modeling the regularly fractured reservoirs, first in the uncoupled flow simulations [28, 29]. Later, for coupled flow and geomechanics, [27] extended poroelasticity of the single porosity model to that of the double porosity model. [25] and [27] proposed constitutive relations in the double porosity systems and the design of the corresponding experiments. The constitutive relations in [25] determine geomechanical and flow properties of a gridblock from the given properties of subelements within the gridblock. On the other hand, extending the single porosity model in [24] to the double porosity model, [30] proposed different constitutive relations from the given geomechanical properties of the gridblock, emphasizing on continuum principles of thermodynamics. Following the approach by [25] and [27], [31] studied thermoporomechanics with the double-porosity concept, using a variant of the undrained sequential method in numerical implementation. However, general formulations and numerical algorithms on thermoporomechanics in multiple porosity materials, which can encompass multiphase flow and plasticity, are still lacking in the previous studies. Even though some discussion was made in [27], numerical development and simulation on coupled flow and geomechanics in the multiple porosity systems have rarely been investigated. In addition, even though the numerical algorithm used in [31] is numerically unconditionally stable, it causes considerable inaccuracy for high coupling strength and may face non-convergence for the incompressible fluid and solid grains [6, 32, 33]. The undrained split method also produces two stiff sub-problems, which require strong linear solvers and high computational cost to solve them [6]. Coupled multiphase flow and geomechanics for fractured media were studied, for example, in [34] and [35], but geomechanical properties of the fractured medium were assumed to be ignored.

With this motivation at hand, in this paper, we investigate coupled flow and geomechanics in multiple porosity systems for regularly fractured or composite reservoirs, generalizing the double porosity model proposed by [27] to the multiple porosity model. We first determine coupling coefficients between fluid flow and geomechanics. Especially, when the off-diagonal terms of the total compressibility matrix associated with the flow problem are zero, a typical formulation in reservoir simulation [28, 36], an upscaled drained bulk modulus of a gridblock used for mechanics is a volume-fraction weighted harmonic average of drained moduli of the materials within a gridblock. Furthermore, using the coupling coefficients and constraints, we determine the upscaled drained elastic/elastoplastic moduli from the moduli of all materials within the gridblock, and find relations between local and global (upscaled) strains, which provide communication between the local and global elastic/plastic variables when mechanics is in the elastic/plastic regime. Additionally, the analyses of poromechanics can immediately be extended to thermomechanics. We will show that all the proposed relations for the multiple porosity model can also generate well-posed problems, just as constitutive relations of the single porosity model (i.e., contractivity). The contractivity implies that the constitutive relations honor the dissipative mechanism in thermodynamics, although an approximation of the upscaling method might not honor conservation laws of mass, energy, or

momentum exactly, which can be accomplished by the fine scale single porosity model that defines the exact configurations of all subelements.

Then, in the numerical implementation, we introduce a sequential implicit method for thermoporomechanics in multiple porosity systems. Specifically, we extend the fixed-stress sequential method for single porosity systems to multiple porosity systems. Introducing a norm for the multiple porosity systems, the fixed-stress sequential method modified for the multiple porosity model still provides unconditional stability (i.e., B-stability), just as the single porosity model rigorously shown in [32, 37]. This sequential scheme can also easily be implemented by constructing an interface between existing flow and geomechanics simulators, introducing the Lagrange porosity function and its corresponding porosity correction term that corrects the inconsistency between the porosity function in flow and strain values in mechanics. The return mapping in modeling elastoplasticity is performed at all materials within a gridblock.

We employ the finite volume/finite element methods for flow and mechanics in space discretization, respectively, and the backward Euler method in time discretization. We implement the proposed formulation and numerical algorithms to TOUGHREACT(flow simulator) coupled to ROCMECH (geomechanics simulator) at Lawrence Berkeley National Laboratory, and test 1D and 2D small scale problems.

From numerical results, we observe clear differences between the single and double/multiple porosity systems such as fracture-rock matrix systems. For example, the fluid pressure in the fracture continuum for the five-porosity model (a model with five interacting porosity systems) becomes higher than that for the single porosity because the bulk modulus of the fracture continuum is lower than the upscaled bulk modulus used in the single porosity. For elastoplasticity, where we adopt the Mohr-Coulomb model, the fluid pressure in the fracture medium can be more supported by compaction when the fracture medium enters the plastic region. In a 2D case of the five-porosity system, we compare results between the conventional uncoupled flow simulation and thermoporoelasticity, and find significant differences between them. We will discuss more details on these complicated physics of coupled problems in the section of numerical examples.

2. MATHEMATICAL FORMULATION

We use a classical continuum representation, where the fluid and solid skeleton are viewed as overlapping continua. The governing equations for heat and fluid flow, and mechanics are obtained from energy, mass and linear-momentum balances, respectively. For multiphase fluid flow, the mass-conservation equation is expressed as

$$\frac{dm_J}{dt} + \mathrm{Div}\, \boldsymbol{w}_J = q_J, \tag{1}$$

where the subscript J denotes a particular fluid phase. m_J is fluid mass, q_J is a source term, $\mathrm{Div}(\cdot)$ is the divergence operator, and $\boldsymbol{w}_J$ is the mass-flux of fluid phase J relative to the motion of the solid skeleton. The accumulation term, dm_J/dt, describes the time variation of fluid mass relative to the motion of the solid skeleton, as well. From here on, we denote by $d(\cdot)/dt$ the change in a quantity $(\cdot)$ relative to the motion of the solid skeleton.

The volumetric flux of phase J, $\boldsymbol{v}_J = (\boldsymbol{w}/\rho)_J$, is given by Darcy's law as

$$\boldsymbol{v}_J = -\frac{\boldsymbol{k}_{p,JK}}{\mu_J}(\mathbf{Grad}\, p_K - \rho_K \boldsymbol{g}), \tag{2}$$

where $\boldsymbol{k}_{p,JK}$ is the effective-permeability tensor (for two fluid phases, J and K). μ_J and ρ_J denote the viscosity and density at the current state for fluid phase J, respectively. $\mathbf{Grad}(\cdot)$ is the gradient operator. Double indices (e.g., K in Equation 2) indicate summation in this section. Typically in reservoir simulation, $\boldsymbol{k}_{p,JK}$ is split into an (absolute) permeability $\boldsymbol{k}_p$ and a relative permeability k^r_{JK}, which is expressed as $\boldsymbol{k}_{p,JK} = \boldsymbol{k}_p k^r_{JK}$, where $k^r_{JK} = 0$ if $J \neq K$.

The governing equation for heat flow comes from energy balance, which is written as

$$\frac{dm^\theta}{dt} + \mathrm{Div}\, \boldsymbol{f}^\theta = q^\theta, \tag{3}$$

where the superscript θ indicates the heat component. m^θ, $\mathbf{f}^\theta$, and q^θ are heat, and its flux and source terms, respectively. The heat m^θ is expressed as

$$m^\theta = (1-\phi)\rho_R C_R T + \phi(S\rho)_J e_J, \tag{4}$$

where ρ_R and C_R are the density and heat capacity of the porous media. S_J is saturation for fluid phase J. T is temperature. e_J is the specific internal energy of phase J. ϕ is the true porosity, defined as the ratio of the pore volume to the bulk volume in the deformed configuration. The heat flux $\boldsymbol{f}^\theta$ is driven by conduction and convection, written as

$$\boldsymbol{f}^\theta = -\left((1-\phi)\mathbf{K}_R + \phi S_J \mathbf{K}_J\right)\mathbf{Grad}\, T + h_J \boldsymbol{w}_J, \tag{5}$$

where $\mathbf{K}_R$ and $\mathbf{K}_J$ are the thermal conductivity tensors of the porous media and fluid phase J, respectively. h_J is the specific enthalpy for phase J.

The governing equation for mechanics is given by the quasi-static assumption as

$$\mathrm{Div}\, \boldsymbol{\sigma} + \rho_b \boldsymbol{g} = \mathbf{0}, \tag{6}$$

where $\boldsymbol{\sigma}$ is the Cauchy total-stress tensor. $\rho_b (= \phi S_J \rho_J + (1-\phi)\rho_R)$ is the bulk density. Here, we assume the infinitesimal transformation, from which the strain tensor is the symmetric gradient of the displacement vector, written as

$$\boldsymbol{\varepsilon} = \mathbf{Grad}^s\, \boldsymbol{u} = \frac{1}{2}(\mathbf{Grad}\, \boldsymbol{u} + \mathbf{Grad}^t\, \boldsymbol{u}), \tag{7}$$

where $\boldsymbol{\varepsilon}$ and $\boldsymbol{u}$ are the strain tensor and the displacement vector, respectively. From here on, tensile stress and strain are positive.

For mathematical completeness, we determine initial and boundary conditions on the domain Ω with the boundary $\partial\Omega$. For fluid flow, we consider the boundary conditions $p_J = \bar{p}_J$ (prescribed pressure) on the boundary Γ_p, and $\boldsymbol{w}_J \cdot \boldsymbol{n} = \bar{w}_J$ (prescribed mass flux) on the boundary Γ_f, where $\Gamma_p \cap \Gamma_f = \emptyset$, and $\Gamma_p \cup \Gamma_f = \partial\Omega$. The boundary conditions for heat flow are $T = \bar{T}$ (prescribed temperature) on the boundary Γ_T, and $\boldsymbol{f}^\theta \cdot \boldsymbol{n} = \bar{f}^\theta$ (prescribed heat flux) on the boundary Γ_θ, where $\Gamma_T \cap \Gamma_\theta = \emptyset$, and $\Gamma_T \cup \Gamma_\theta = \partial\Omega$. The boundary conditions for the mechanical problem are $\boldsymbol{u} = \bar{\boldsymbol{u}}$ (prescribed displacement) on the boundary Γ_u and $\boldsymbol{\sigma} \cdot \boldsymbol{n} = \bar{\boldsymbol{t}}$ (prescribed traction) on the boundary Γ_σ, where $\Gamma_u \cap \Gamma_\sigma = \emptyset$, and $\Gamma_u \cup \Gamma_\sigma = \partial\Omega$. The initial stress field should satisfy mechanical and thermodynamic equilibriums, and be consistent with the fluid pressure, temperature, and history of the stress-strain paths. Here, we take the initial conditions of the coupled problem as $p_J|_{t=0} = p_{J,0}$, $T|_{t=0} = T_0$, and $\boldsymbol{\sigma}|_{t=0} = \boldsymbol{\sigma}_0$.

3. DISCRETIZATION

In this study we use a mixed space discretization. We employ the finite volume method for fluid and heat flow in space discretization, typically used in reservoir simulation [36, 38, 39], where pressure and temperature are located at the cell center (the left of Figure 1). On the other hand, space discretization for mechanics is based on a nodal-based finite-element method, widely used

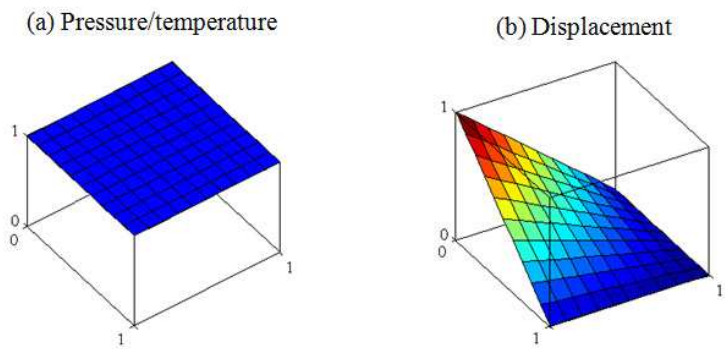

Figure 1. Element shape functions for (a) pressure and temperature (left) and (b) displacement (right) in 2-D. The pressure/temperature and displacement fields are approximated with piecewise constant and piecewise continuous interpolation functions, respectively.

in mechanical and geotechnical engineering, where the displacement vector is located at vertices, shown in (the right of Figure 1) [40].

This mixed space discretization has (1) local mass and heat conservations at the element level, (2) continuous displacement field, which allows for tracking the deformation, (3) convergent approximations with the lowest order discretization [41], and (4) relatively stable approximations, compared with a piecewise continuous interpolation for fluid pressure when we use the finite element method for flow [8, 41, 42, 43]. In time discretization, we use the backward Euler method. We use TOUGHREACT and ROCMECH simulators, developed in Lawrence Berkeley National Laboratory, for fluid-heat flow and geomechanics, respectively [39]. These simulators adopt the aforementioned space and time discretizations.

4. CONSTITUTIVE RELATIONS FOR SINGLE POROSITY SYSTEMS

The constitutive relations for thermoporomechanics in a single porosity model are based on [18], [21], and [44], where fluid, heat, and mechanics are tightly coupled. The total stress $\boldsymbol{\sigma}$, fluid mass m_J, and entropy $\bar{S}$ in the elastic coupled system are functions of the total strain ε, fluid pressure p_J, and temperature T, written as

$$\delta\boldsymbol{\sigma} = \underbrace{\mathbf{C}_{dr} : \delta\boldsymbol{\varepsilon}}_{\delta\boldsymbol{\sigma}'} - \alpha_J \delta p_J \mathbf{1} - 3\alpha_T K_{dr} \delta T \mathbf{1}, \tag{8}$$

$$\left(\frac{\delta m}{\rho}\right)_J = \alpha_J \delta\varepsilon_v + N_{JK}\delta p_K - 3\alpha_{m,J}\delta T, \tag{9}$$

$$\delta\bar{S} = \bar{s}_J \delta m_J + 3\alpha_T K_{dr}\delta\boldsymbol{\varepsilon}_v - 3\alpha_{m,J}\delta p_J + \frac{C_d}{T}\delta T, \tag{10}$$

where $\mathbf{C}_{dr}$ is the drained-isothermal elastic moduli, $\mathbf{N} = \{N_{JK}\}$ is the inverse matrix of the Biot moduli $\mathbf{M} = \{M_{JK}\}$ (i.e., $\mathbf{N} = \mathbf{M}^{-1}$), where $\mathbf{N}$ and $\mathbf{M}$ are positive definite. The Biot coefficient α_J for multiphase flow takes $\alpha_J = \alpha S_J$, where α is the Biot coefficient for single phase flow [20]. We define $\boldsymbol{\sigma'}$, the effective stress, in the incremental form as $\delta\boldsymbol{\sigma'} = \mathbf{C}_{dr} : \delta\boldsymbol{\varepsilon}$, where $\boldsymbol{\sigma'} = \mathbf{0}$ at $\boldsymbol{\varepsilon} = \mathbf{0}$. $3\alpha_T$ is the volumetric skeleton thermal dilation coefficient, K_{dr} is the drained isothermal bulk modulus, $\mathbf{1}$ is the rank-2 identity tensor, ε_v is the total volumetric strain, and $3\alpha_{m,J} = 3\alpha_\phi + \phi 3\alpha_J$, where $3\alpha_\phi$ and $3\alpha_J$ are the coefficients of thermal dilation related to porosity and phase J, respectively. $\bar{s}_J$ is the internal entropy per unit mass of phase J (i.e., specific entropy of phase J). $C_d = C + m_J C_{p,J}$ is the total volumetric heat capacity, where C is the skeleton volumetric heat capacity and $C_{p,J}$ is the volumetric specific heat capacity at constant pressure for phase J. Double

indices in Equations 8 – 10 indicate summation. δ implies variation relative to the motion of the solid skeleton.

For a two-phase fluid system (such as oil and water), an appropriate (i.e., admissible) $\mathbf{N}$, which is typically used in engineering, is given as (e.g., [22])

$$\mathbf{N} = \begin{bmatrix} \phi S_o c_o - \phi \dfrac{dS_w}{dp_{co}} + S_o \dfrac{b-\phi}{K_s} S_o & \phi \dfrac{dS_w}{dp_{co}} + S_o \dfrac{b-\phi}{K_s} S_w \\ \phi \dfrac{dS_w}{dp_{co}} + S_w \dfrac{b-\phi}{K_s} S_o & \phi S_w c_w - \phi \dfrac{dS_w}{dp_{co}} + S_w \dfrac{b-\phi}{K_s} S_w \end{bmatrix}, \tag{11}$$

where the subscript $(\cdot)_o$ indicates the oil phase, c_J is the compressibility of the fluid phase J, p_{co} is the capillary pressure between oil and water, and K_s is the intrinsic solid grain bulk modulus.

Equations 8– 10 and the corresponding definition of effective stress honor the first and second thermodynamic laws in physics and, in mathematics, provide wellposed problems and unconditional numerical stability when fully coupled methods are used [21, 37, 44].

5. EXTENSION TO MULTIPLE POROSITY SYSTEMS

5.1. Poroelasticity

The single porosity theory in poromechanics has limited applicability for fractured or composite reservoirs because they are highly heterogeneous within a gridblock, a representative elementary volume [25, 26, 27]. To overcome such limitations, the double porosity (also called dual porosity) model was proposed and investigated, introducing dual continua such as fracture and rock matrix porous media.

[25] and [27] extended the single porosity theory of poromechanics in isothermal single fluid phase to the double porosity model, and determined the coupling coefficients. The constitutive relations proposed by [27] are

$$\begin{pmatrix} \delta\varepsilon_v \\ \delta\zeta \end{pmatrix} = \begin{pmatrix} a & -\mathbf{b}^T \\ -\mathbf{b} & \mathbf{D} \end{pmatrix} \begin{pmatrix} \delta\sigma_v \\ \delta\mathbf{p} \end{pmatrix}, \tag{12}$$

$$\zeta = \begin{pmatrix} \zeta_f \\ \zeta_m \end{pmatrix}, \ \mathbf{p} = \begin{pmatrix} p_f \\ p_m \end{pmatrix}, \ \mathbf{b} = \begin{pmatrix} b_f \\ b_m \end{pmatrix}, \mathbf{D} = \begin{pmatrix} d_{ff} & d_{fm} \\ d_{mf} & d_{mm} \end{pmatrix}, \tag{13}$$

where σ_v is the total volumetric (mean) stress (i.e., $\mathrm{tr}\boldsymbol{\sigma}/3$), and the subscripts f and m indicate fracture and rock matrix media, respectively. ζ implies the fluid content at each medium, where $\delta\zeta = \delta m/\rho$. The coefficients of a, $\mathbf{b}$, and $\mathbf{D}$ are expressed as

$$a = \frac{1}{K_{dr}}, \ b_f = \frac{\alpha_f}{K_f}\frac{1-K_m/K_{dr}}{1-K_m/K_f}, \ b_m = \frac{\alpha_m}{K_m}\frac{1-K_f/K_{dr}}{1-K_f/K_m}, \tag{14}$$

$$d_{ff} = \frac{\eta_f \alpha_f}{B_f K_f} - \left(\frac{\alpha_f}{1-K_f/K_m}\right)^2 \left(\frac{\eta_f}{K_f} + \frac{\eta_m}{K_m} - \frac{1}{K_{dr}}\right), \tag{15}$$

$$d_{mm} = \frac{\eta_m \alpha_m}{B_m K_m} - \left(\frac{\alpha_m}{1-K_m/K_f}\right)^2 \left(\frac{\eta_m}{K_m} + \frac{\eta_f}{K_f} - \frac{1}{K_{dr}}\right), \tag{16}$$

$$d_{fm} = \frac{K_f K_m \alpha_f \alpha_m}{(K_m - K_f)^2} \left(\frac{\eta_m}{K_m} + \frac{\eta_f}{K_f} - \frac{1}{K_{dr}}\right), \ d_{mf} = d_{fm}, \tag{17}$$

where K_f, α_f, B_f and η_f are the drained bulk modulus, Biot coefficient, and Skempton coefficient, volume fraction of the fracture medium, while K_m, α_m, B_m, and η_m are those corresponding to the

rock matrix medium. For example, the Biot and Skempton coefficients for the fracture are defined as

$$\alpha_f = 1 - \frac{K_f}{K_s}, \;\; B_f = \frac{M_f \alpha_f}{K_f + \alpha_f^2 M_f}, \;\; \frac{1}{M_f} = \phi c_f + \frac{\alpha_f - \phi}{K_s}, \tag{18}$$

where c_f is the intrinsic fluid compressibility, and M_f is the Biot modulus.

K_{dr} is a drained bulk modulus of a gridblock used for mechanics, upscaled from drained bulk moduli of the fracture and rock matrix media within a gridblock. $\mathbf{b}$ is the coupling coefficient vector between fluid flow and mechanics. $\mathbf{D}$ implies the coupling coefficient matrix between fluid variables, which corresponds to the total compressibility matrix in conventional reservoir simulation.

[27] discussed a possible extension of the double porosity constitutive model to the multiple porosity system, and concluded that the uniform expansion and contraction scenario can carry over to the multiple porosity model just as it does in the double porosity model, but that the extension to the multiple porosity model still remains an open question because the scenario does not provide the sufficient equations to determine all the coefficients of the constitutive relations.

In this section, we focus on determining the coupling coefficients between fluid flow and mechanics in the multiple porosity system, as shown in Figure 2, assuming the coefficients between fluid flow variables (i.e., $\mathbf{D}$) to be given. To this end, we first introduce the same form of the constitutive relations of the double porosity model as follows.

$$\begin{pmatrix} \delta\varepsilon_v \\ \delta\zeta \end{pmatrix} = \begin{pmatrix} a & -\mathbf{b}^T \\ -\mathbf{b} & \mathbf{D} \end{pmatrix} \begin{pmatrix} \delta\sigma_v \\ \delta\mathbf{p} \end{pmatrix}, \tag{19}$$

$$\zeta = \begin{pmatrix} \zeta_1 \\ \vdots \\ \zeta_{\mathrm{n}_m} \end{pmatrix}, \mathbf{p} = \begin{pmatrix} p_1 \\ \vdots \\ p_{\mathrm{n}_m} \end{pmatrix}, \mathbf{b} = \begin{pmatrix} b_1 \\ \vdots \\ b_{\mathrm{n}_m} \end{pmatrix}, \mathbf{D} = \begin{pmatrix} d_{11} & \cdots & d_{1\mathrm{n}_m} \\ \vdots & \ddots & \vdots \\ d_{\mathrm{n}_m 1} & \cdots & d_{\mathrm{n}_m \mathrm{n}_m} \end{pmatrix}, \tag{20}$$

where n_m is the number of materials per gridblock. $\mathbf{D}$ is known from the assumption that the coefficients between fluid pressure and mass are given. This assumption is relevant because $\mathbf{D}$ represents interrelations between fluid pressures of different materials in the fluid flow simulation uncoupled to mechanics (i.e., total compressibility matrix of the multiple porosity model), determined by a given formulation of the flow problem itself. Double indices do not indicate summation in this section. We specify the summation symbol Σ separately. We call 'sub-element' an element occupied by a material within a gridblock (e.g., fracture or rock matrix).

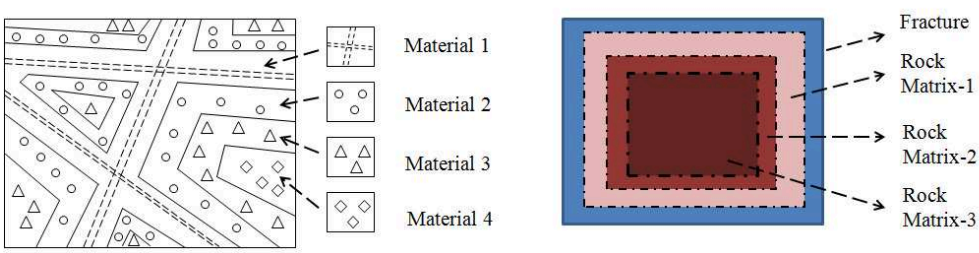

Figure 2. Schematic diagrams for the multiple porosity model. Left: a composite porous medium which consists of several distinct types of porous materials. Right: a conceptual diagram of the MINC model, as an example of the multiple porosity model [28].

Consider that each material is assumed to be what we call "Gassmann material" [27], a microhomogeneous porous medium, satisfying

$$\begin{pmatrix} \delta\varepsilon_v^k \\ \delta\zeta_k/\eta_k \end{pmatrix} = \frac{1}{K_k} \begin{pmatrix} 1 & \alpha_k \\ \alpha_k & \alpha_k/B_k \end{pmatrix} \begin{pmatrix} \delta\sigma_v^k \\ \delta p_k \end{pmatrix}, \tag{21}$$

where the subscript or superscript k means a material index. η_k is the volume fraction of material k within a gridblock. Considering the uniform expansion and contraction scenario just as used in the double porosity model [27], we obtain

$$\delta\varepsilon_v = \delta\varepsilon_v^1 = \cdots = \delta\varepsilon_v^k = \cdots = \delta\varepsilon_v^{\mathrm{n}_m}, \tag{22}$$

$$\delta\sigma_v = \delta\sigma_v^1 = \cdots = \delta\sigma_v^k = \cdots = \delta\sigma_v^{\mathrm{n}_m}. \tag{23}$$

Then, Equations 22 and 23 provide

$$\frac{1}{K_k}\left(\delta\sigma_v + \alpha_k\delta p_k\right) = \frac{1}{K_l}\left(\delta\sigma_v + \alpha_l\delta p_l\right), \;\; (k \neq l), \;\; k, l = 1, \cdots, \mathrm{n}_m, \tag{24}$$

where the subscript l is another material index. Rearranging Equation 24, we obtain

$$\delta p_l = -\frac{1}{\alpha_l}\left\{\left(1 - \frac{K_l}{K_k}\right)\delta\sigma_v - \frac{K_l}{K_k}\alpha_k\delta p_k\right\}. \tag{25}$$

Note that $a = 1/K_{dr}$, already obtained from the double porosity model, shown in Equation 14. The first row of Equation 19 can be rewritten by using Equation 25 as

$$\begin{aligned} \delta\varepsilon_v &= \frac{1}{K_{dr}}\delta\sigma_v - \sum_{l=1}^{\mathrm{n}_m} b_l\delta p_l \\ &= \frac{1}{K_{dr}}\delta\sigma_v + \sum_{l=1}^{\mathrm{n}_m} b_l\frac{1}{\alpha_l}\left\{\left(1 - \frac{K_l}{K_k}\right)\delta\sigma_v - \frac{K_l}{K_k}\alpha_k\delta p_k\right\}. \end{aligned} \tag{26}$$

Then, based on the uniform expansion and contraction scenario of Equations 22 and 23, Equation 26 must be identical to the first row in Equation 21. Comparing two equations, we obtain

$$\frac{1}{K_k} = \frac{1}{K_{dr}} + \sum_{l=1}^{\mathrm{n}_m} b_l\frac{1}{\alpha_l}\left(1 - \frac{K_l}{K_k}\right), \tag{27}$$

$$\sum_{l=1}^{\mathrm{n}_m} b_l\frac{K_l}{\alpha_l} = -1. \tag{28}$$

We can also substitute Equation 25 into the mass content term (i.e., $\delta\zeta$) of Equation 19, and this leads to

$$\delta\zeta_k = -b_k\delta\sigma_v - \sum_{l=1}^{\mathrm{n}_m} d_{kl}\frac{1}{\alpha_l}\left\{\left(1 - \frac{K_l}{K_k}\right)\delta\sigma_v - \frac{K_l}{K_k}\alpha_k\delta p_k\right\}. \tag{29}$$

Considering the uniform expansion and contraction scenario, again, and comparing Equation 29 with the second row of Equation 21, we obtain

$$b_k = -\alpha_k \frac{\eta_k}{K_k} - \sum_{l=1}^{\mathrm{n}_m} d_{kl} \frac{1}{\alpha_l} \left(1 - \frac{K_l}{K_k}\right), \tag{30}$$

$$\sum_{l=1}^{\mathrm{n}_m} d_{kl} \frac{K_l}{\alpha_l} \frac{\alpha_k}{K_k} = \frac{\eta_k}{K_k} \frac{\alpha_k}{B_k}. \tag{31}$$

Thus, the coupling coefficient b_k is determined from Equation 30 because d_{kl}, K_k, K_l, α_k, α_l, and η_k are known. Accordingly, K_{dr} is determined from Equation 27. Equations 28 and 31 are the constraints that also need to be satisfied.

Typically, the off-diagonal terms of $\mathbf{D}$ are zero in the conventional flow formulation for the multiple porosity model (i.e., $d_{kl} = 0$ when $k \neq l$) [28]. Then, this condition yields from Equations 30, 31, and 27, respectively,

$$b_k = -\alpha_k \frac{\eta_k}{K_k}, \;\; d_{kk} = \frac{\eta_k}{K_k} \frac{\alpha_k}{B_k}, \;\; \frac{1}{K_{dr}} = \sum_{k=1}^{\mathrm{n}_m} \frac{\eta_k}{K_k}, \tag{32}$$

from which the constraint, Equation 28, is immediately satisfied. Note that K_{dr} is the volume-fraction weighted harmonic average of drained bulk moduli of sub-elements. This is consistent with the conventional up-scaling method in compressibility. Hereafter, we take the assumption that the off-diagonal terms of $\mathbf{D}$ are zero, unless noted otherwise.

5.2. Thermoelasticity

We can determine coupling between heat flow and geomechanics in the double/multiple porosity systems, just as coupling between fluid flow and geomechanics. Let us introduce the same form of Equations 19 and 20 as

$$\begin{pmatrix} \delta\varepsilon_v \\ \delta\bar{\mathbf{S}} \end{pmatrix} = \begin{pmatrix} a & -\tilde{\mathbf{b}}^T \\ -\tilde{\mathbf{b}} & \tilde{\mathbf{D}} \end{pmatrix} \begin{pmatrix} \delta\sigma_v \\ \delta\mathbf{T} \end{pmatrix}, \tag{33}$$

$$\bar{\mathbf{S}} = \begin{pmatrix} \bar{S}_1 \\ \vdots \\ \bar{S}_{\mathrm{n}_m} \end{pmatrix}, \mathbf{T} = \begin{pmatrix} T_1 \\ \vdots \\ T_{\mathrm{n}_m} \end{pmatrix}, \tilde{\mathbf{b}} = \begin{pmatrix} \tilde{b}_1 \\ \vdots \\ \tilde{b}_{\mathrm{n}_m} \end{pmatrix}, \tilde{\mathbf{D}} = \begin{pmatrix} \tilde{d}_{11} & \cdots & \tilde{d}_{1\mathrm{n}_m} \\ \vdots & \ddots & \vdots \\ \tilde{d}_{\mathrm{n}_m 1} & \cdots & \tilde{d}_{\mathrm{n}_m \mathrm{n}_m} \end{pmatrix}, \tag{34}$$

where $\tilde{\mathbf{D}}$ is assumed to be known from a heat flow model. This assumption is, again, relevant because $\tilde{\mathbf{D}}$ represents relations between temperatures of all materials in the heat flow simulation uncoupled to mechanics, (i.e., total heat capacity matrix), determined by a given formulation of the heat flow problem itself.

When we consider Equations 8 – 10 without fluid flow, the constitutive relations of thermoelasticity for the single porosity model read

$$\begin{pmatrix} \delta\varepsilon_v \\ \delta\bar{S} \end{pmatrix} = \frac{1}{K_{dr}} \begin{pmatrix} 1 & \gamma \\ \gamma & \gamma/\tilde{B} \end{pmatrix} \begin{pmatrix} \delta\sigma_v \\ \delta T \end{pmatrix}, \;\; \gamma = 3\alpha_T K_{dr}, \;\; \frac{1}{\tilde{B}} = \frac{C_{is}}{3\alpha_T T}, \tag{35}$$

where $C_{is} = C_d + 9\alpha_T^2 K_{dr} T$ is the volumetric heat capacity at constant stress [44]. We identify that Equation 35 is the same form as the constitutive relations in coupling between fluid flow and geomechanics, when the Biot and Skempton coefficients (i.e., b and B, respectively) for single fluid phase in poroelasticity are substituted by γ and $\tilde{B}$ in thermoelasticity, respectively.

Thus, when determining the coupling coefficients of thermoelasticity in double and multiple porosity systems, we can employ the same procedure and results previously shown in coupling between fluid flow and geomechanics, simply replacing the Biot and Skempton coefficients with γ and $\tilde{B}$. In particular, when the off-diagonal terms in $\tilde{\mathbf{D}}$ are zero, we obtain

$$\tilde{b}_k = -\gamma_k \frac{\eta_k}{K_k}, \;\; \tilde{d}_{kk} = \frac{\eta_k}{K_k}\frac{\gamma_k}{\tilde{B}_k}. \tag{36}$$

5.3. Determination of drained elasticity tensor $\mathbf{C}_{dr}$ and local strain $\boldsymbol{\varepsilon}_k$

The stress-strain relation for mechanics in the multiple porosity model can be written, replacing σ_v and K_{dr} of Equation 19 with $\boldsymbol{\sigma}$ and $\mathbf{C}_{up}$, in a tensorial form as

$$\delta\boldsymbol{\sigma} \;\; = \;\; \mathbf{C}_{up} : \delta\boldsymbol{\varepsilon} + \sum_{l=1}^{\mathrm{n}_m} b_l \delta p_l \mathbf{1}, \tag{37}$$

where $\mathbf{C}_{up}$ is a drained elasticity tensor of the mechanics problem to be upscaled and determined from the materials of sub-elements within a gridblock as follows.

We reuse the uniform expansion and contraction scenario shown in Equations 22 and 23, and replace the volumetric stress and strain with the total stress and strain tensors, respectively. Then, the relations among the total stress, strain, and pore-pressure can be written as

$$\delta\boldsymbol{\sigma} \;\; = \;\; \mathbf{C}_k : \delta\boldsymbol{\varepsilon} - \alpha_k \delta p_k \mathbf{1} \tag{38}$$

$$\;\; = \;\; \mathbf{C}_l : \delta\boldsymbol{\varepsilon} - \alpha_l \delta p_l \mathbf{1}, \;\; (k \neq l), \;\; k, l = 1, \cdots, \mathrm{n}_m, \tag{39}$$

where $\mathbf{C}_k$ and $\mathbf{C}_l$ are drained elasticity tensors for materials k and l, respectively. Rearranging Equation 38, we obtain

$$\delta p_l \mathbf{1} = \frac{1}{\alpha_l} \left\{ (\mathbf{C}_l - \mathbf{C}_k) : \delta\boldsymbol{\varepsilon} + \alpha_k \delta p_k \mathbf{1} \right\}. \tag{40}$$

Substituting Equation 40 into Equation 37,

$$\delta\boldsymbol{\sigma} = \mathbf{C}_{up} : \delta\boldsymbol{\varepsilon} + \sum_{l=1}^{\mathrm{n}_m} b_l \frac{1}{\alpha_l} \left\{ (\mathbf{C}_l - \mathbf{C}_k) : \delta\boldsymbol{\varepsilon} + \alpha_k \delta p_k \mathbf{1} \right\}. \tag{41}$$

Comparing Equation 41 with Equation 38 and using Equation 32_1, we obtain

$$\mathbf{C}_k = \mathbf{C}_{up} + \sum_{l=1}^{\mathrm{n}_m} \frac{\eta_l}{K_l} \left(\mathbf{C}_k - \mathbf{C}_l \right). \tag{42}$$

Let us multiply both sides of Equation 42 by η_k / K_k and take summation from $k = 1$ to $k = \mathrm{n}_m$. Then, rearranging the equation, we have

$$\underbrace{\sum_{k=1}^{\mathrm{n}_m} \frac{\eta_k}{K_k}}_{1/K_{dr}} \mathbf{C}_{up} = \sum_{k=1}^{\mathrm{n}_m} \frac{\eta_k}{K_k} \mathbf{C}_k + \underbrace{\sum_{k=1}^{\mathrm{n}_m} \frac{\eta_k}{K_k}}_{1/K_{dr}} \left(\sum_{l=1}^{\mathrm{n}_m} \frac{\eta_l}{K_l} \mathbf{C}_l \right) - \sum_{k=1}^{\mathrm{n}_m} \frac{\eta_k}{K_k} \mathbf{C}_k \underbrace{\sum_{l=1}^{\mathrm{n}_m} \frac{\eta_l}{K_l}}_{1/K_{dr}}, \tag{43}$$

which yields, using Equation 32_3,

$$\mathbf{C}_{up} = K_{dr} \sum_{k=1}^{\mathrm{n}_m} \frac{\eta_k}{K_k} \mathbf{C}_k. \tag{44}$$

Let us assume that variations in the global effective stress $\delta\boldsymbol{\sigma'}$ (i.e., gridblock effective stress) can be determined from the sum of volume fraction weighted variations in effective stresses of the materials of sub-elements (i.e., $\eta_k \delta\boldsymbol{\sigma'}_k$), expressed as

$$\delta\boldsymbol{\sigma'} = \sum_{k=1}^{\mathrm{n}_m} \eta_k \delta\boldsymbol{\sigma'}_k, \tag{45}$$

which is the same type of the definition in pore-pressure for multiple fluid phases (i.e., equivalent pore-pressure p_E, where $\delta p_E = \sum S_J \delta p_J$) [5, 37, 44]. Using Equation 44 and considering the local effective stress-strain constitutive relation (i.e., $\delta\boldsymbol{\sigma'}_k = \mathbf{C}_k : \delta\boldsymbol{\varepsilon}_k$), we obtain from Equation 45

$$\delta\boldsymbol{\sigma'} = \frac{K_{dr}}{K_k} \mathbf{C}_k : \delta\boldsymbol{\varepsilon}, \;\; \delta\boldsymbol{\varepsilon}_k = \frac{K_{dr}}{K_k} \delta\boldsymbol{\varepsilon}. \tag{46}$$

5.4. Poroelastoplasticity

Changes in total-stress and fluid pressure in elastoplasticity for single fluid phase and isothermal conditions are related to changes in strain and fluid content as follows [21, 44]:

$$\delta\boldsymbol{\sigma} = \underbrace{\mathbf{C}_{dr} : (\delta\boldsymbol{\varepsilon} - \delta\boldsymbol{\varepsilon}_p)}_{\delta\boldsymbol{\sigma'}} - \alpha\delta p\mathbf{1}, \tag{47}$$

$$\delta p = M \left(-\alpha(\delta\varepsilon_v - \delta\varepsilon_{v,p}) + \underbrace{(\delta\zeta - \delta\phi_p)}_{\delta\zeta_e} \right), \tag{48}$$

where $\delta\zeta_e$ is the variation of the elastic fluid content of phase J. The subscripts e and p denote elasticity and plasticity, respectively. The plastic porosity ϕ_p and plastic volumetric strain $\varepsilon_{v,p}$ can be related to each other by assuming that [6]

$$\delta\phi_p = \alpha\delta\varepsilon_{v,p}. \tag{49}$$

Then, introducing elastoplastic tangent moduli $\mathbf{C}_{up}^{ep}$ into Equation 47 [45], Equations 47 and 48 can be rewritten as

$$\delta\boldsymbol{\sigma} = \mathbf{C}_{dr}^{ep} : \delta\boldsymbol{\varepsilon} - \alpha\delta p\mathbf{1}, \tag{50}$$

$$\delta p = M\left(-\alpha\delta\varepsilon_v + \delta\zeta\right), \tag{51}$$

where the superscript 'ep' implies elastoplasticity. Note that Equations 50 and 51 are expressed by total stress/strain and total fluid mass/fluid pressure. Thus, we can extend the previous analyses of elasticity to elastoplasticity immediately. Accordingly, α in Equations 50 and 51 for elastoplasticity becomes $\alpha = 1 - K_{dr}^{ep}/K_s$, where K_{dr}^{ep} is the drained elastoplastic bulk modulus. Furthermore, we rewrite Equation 32 as

$$b_k = -\alpha_k \frac{\eta_k}{K_k^{ep}}, \;\; d_{kk} = \frac{\eta_k}{K_k^{ep}} \frac{\alpha_k}{B_k^{ep}}, \;\; \frac{1}{K_{dr}^{ep}} = \sum_{k=1}^{\mathrm{n}_m} \frac{\eta_k}{K_k^{ep}}, \tag{52}$$

where we use the elastoplastic drained bulk modulus in the coupling coefficient b_k instead of the elastic drained bulk modulus. Then the gridblock elastoplastic tangent moduli upscaled from the materials of sub-elements can be obtained as

$$\mathbf{C}_{up}^{ep} = K_{dr}^{ep} \sum_{k=1}^{\mathrm{n}_m} \frac{\eta_k}{K_k^{ep}} \mathbf{C}_k^{ep}. \tag{53}$$

According to Equation 46, the local effective stress, elastic and total strains of material k are determined, respectively, as

$$\delta \boldsymbol{\sigma'}_k = \frac{K_{dr}^{ep}}{K_k^{ep}} \mathbf{C}_k^{ep} : \delta\boldsymbol{\varepsilon}, \;\; \delta\boldsymbol{\varepsilon}_k^e = \frac{K_{dr}^{e}}{K_k^{e}} \delta\boldsymbol{\varepsilon}^e, \;\; \delta\boldsymbol{\varepsilon}_k = \frac{K_{dr}^{ep}}{K_k^{ep}} \delta\boldsymbol{\varepsilon}, \tag{54}$$

where the superscript e implies elasticity. As a result, the local and global plastic strains are related as follows:

$$\delta\boldsymbol{\varepsilon}_k^p = \left(\frac{K_{dr}^{ep}}{K_k^{ep}} - \frac{K_{dr}^{e}}{K_k^{e}} \right) \delta\boldsymbol{\varepsilon} + \frac{K_{dr}^{e}}{K_k^{e}} \delta\boldsymbol{\varepsilon}^p. \tag{55}$$

6. A SEQUENTIAL SCHEME IN NUMERICAL SIMULATION

6.1. The fixed-stress sequential method and porosity correction

We consider numerical algorithms to solve coupled flow and geomechanics combined with the constitutive relations proposed in this study. Let us assume the off-diagonal terms in $\mathbf{D}$ of Equation 20 to be zero, following the conventional flow formulation for the multiple porosity model, such as MINC [28]. Then, the second row in Equation 19 can be written as

$$\delta\zeta_l = -b_l \delta\sigma_v + \eta_l \left(\frac{\alpha_l^2}{K_l} + \frac{1}{M_l} \right) \delta p_l. \tag{56}$$

In the conventional reservoir simulation for flow only [36], the accumulation of the fluid mass is formulated as

$$\delta m_l = \rho_l \eta_l \left(\delta\Phi_l + \Phi_l c_f \delta p_l \right), \tag{57}$$

where Φ_l is Lagrange's porosity for material l, defined as the ratio of the pore volume in the deformed configuration to the bulk volume in the reference (initial) configuration [23]. Comparing Equation 56 with Equation 57, Lagrange's porosity can be written as

$$\delta\Phi_l = \left(\frac{\alpha_l^2}{K_l} + \frac{\alpha_l - \phi_l}{K_s} \right) \delta p_l - \frac{b_l}{\eta_l} \delta\sigma_v, \tag{58}$$

where ϕ_l may be replaced by Φ_l because the difference can be ignored [14].

Then, we employ the fixed-stress sequential method for a stable and convergent sequential method [33], which will be discussed in Sections 6.3 and 6.4. This method splits the original operator into the two subproblems (i.e., flow and mechanics) as

$$\begin{bmatrix} \boldsymbol{u}^n \\ \boldsymbol{p}_l^n \end{bmatrix} \xrightarrow{\mathcal{A}_{ss}^p} \begin{bmatrix} \boldsymbol{u}^* \\ \boldsymbol{p}_l^{n+1} \end{bmatrix} \xrightarrow{\mathcal{A}_{ss}^u} \begin{bmatrix} \boldsymbol{u}^{n+1} \\ \boldsymbol{p}_l^{n+1} \end{bmatrix}, \quad \text{where} \quad \begin{cases} \mathcal{A}_{ss}^p : \dot{m}_l + \mathrm{Div}\, \boldsymbol{w}_l = (\rho f)_l, \; \delta\dot{\sigma} = 0, \\ \mathcal{A}_{ss}^u : \mathrm{Div}\, \boldsymbol{\sigma} + \rho_b \boldsymbol{g} = \mathbf{0}, \; p_l : \text{prescribed}, \end{cases} \tag{59}$$

where the initial condition of the flow problem $\mathcal{A}^p_{ss}$ is determined from the original coupled problem satisfying

$$\mathrm{Div}\,\dot{\sigma}_{t=0} = 0\,, \quad \mathrm{Div}\,\sigma_{t=0} + \rho_b \boldsymbol{g} = 0. \tag{60}$$

In this fixed-stress split method, when we solve the flow problem $\mathcal{A}^p_{ss}$, we evaluate the term associated with the total volumetric (mean) stress in Equation 58 explicitly. Thus, the fixed-stress split method yields from Equation 58 and the first row of Equation 19

$$\Phi^{n+1} - \Phi^n = \left(\frac{\alpha_l^2}{K_l} + \frac{\alpha_l - \Phi^n}{K_s}\right)\left(p^{n+1}_{l,J} - p^n_{l,J}\right) - \Delta\Phi^l_c, \tag{61}$$

$$\Delta\Phi^l_c = \frac{b_l}{\eta_l}\underbrace{K_{dr}\left\{\left(\varepsilon^n_v - \varepsilon^{n-1}_v\right) - \sum_{k=1}^{\mathrm{n}_m} b_k\left(p^n_k - p^{n-1}_k\right)\right\}}_{\left(\sigma^n_v - \sigma^{n-1}_v\right)}, \tag{62}$$

where the superscript n indicates time level in time discretization, and $\Delta\Phi^l_c$ is called *porosity correction*. We use the coupling coefficient b_k described in Equation 32 because the off-diagonal terms of $\mathbf{D}$ are zero. The Lagrange porosity function and correction modified for the multiple porosity model (i.e., Equations 61 and 62) can easily be implemented in conventional reservoir simulators. Furthermore, the calculation of the porosity correction is local, so the computational cost is negligible, compared with the global calculation, such as linear (matrix) solvers.

6.2. Multiphase flow with elastoplasticity

Considering constitutive relations for single porosity systems with elastoplasticity [6, 21, 44], the previously described constitutive relations can be extended to those of multiphase flow systems with elastoplasticity for the multiple porosity model, as follows.

$$\delta\boldsymbol{\sigma} = \overbrace{\mathbf{C}_{up} : \delta\underbrace{(\boldsymbol{\varepsilon} - \boldsymbol{\varepsilon}_p)}_{\boldsymbol{\varepsilon}_e}}^{\delta\boldsymbol{\sigma}'} - b^*_{l,J}\delta p_{l,J}\mathbf{1}, \;\; b^*_{l,J} = -K_{dr} b_l S_{l,J} \tag{63}$$

$$\underbrace{\delta\zeta_{l,J} - \delta\phi_{(l,J)_p}}_{\delta\zeta_{(l,J)_e}} = b^*_{l,J}\delta\varepsilon_{v,e} + L^{-1}_{l,J,m,I}\delta p_{m,I}, \tag{64}$$

$$\delta\boldsymbol{\kappa}_l = -\mathbf{H}_l \cdot \delta\boldsymbol{\xi}_l, \tag{65}$$

where the subscripts e and p denote elasticity and plasticity, respectively. In this section, we retrieve double indices to indicate summation. $\boldsymbol{\varepsilon}_e$ and $\boldsymbol{\varepsilon}_p$ are the elastic and plastic strains, respectively. $\boldsymbol{\kappa}_l$ and $\boldsymbol{\xi}_l$ are the internal stress-like and strain-like plastic variables for material l, respectively. $\mathbf{H}_l$ is a positive definite hardening modulus matrix for material l. $\zeta_{(l,J)_e}$ and $\phi_{(l,J)_p}$ are the elastic and plastic fluid contents for the material l and phase J, respectively. Similar to the previous single phase flow and single porosity model, we take

$$\delta\phi_{(l,J)_p} = b^*_{l,J}\delta\varepsilon_{v,p}. \tag{66}$$

$\mathbf{L} = \{L_{l,J,m,I}\}$ is a positive-definite tensor, extended from the Biot modulus in single phase flow. For example, when $d_{ij} = 0, i \neq j$, $\mathbf{L}$ for an oil-water phase with a fracture-rock matrix (double porosity) system can be written in a matrix form as

$$\mathbf{L}^{-1} = \begin{bmatrix} \eta_f \mathbf{N}_f & \mathbf{0} \\ \mathbf{0} & \eta_m \mathbf{N}_m \end{bmatrix}, \tag{67}$$

where $\mathbf{N}_f$ and $\mathbf{N}_m$ become the same as $\mathbf{N}$ in Equation 11, when replacing α of Equation 11 with α_f and α_m, respectively. Accordingly, Equations 63 and 64 can be rewritten, respectively, as

$$\delta\boldsymbol{\sigma} = \overbrace{\mathbf{C}_{dr}^{ep}\delta\boldsymbol{\varepsilon}}^{\delta\boldsymbol{\sigma}'} - b_{l,J}^{*}\delta p_{l,J}\mathbf{1}, \tag{68}$$

$$\delta\zeta_{l,J} = b_{l,J}^{*}\delta\varepsilon_v + L_{l,J,m,I}^{-1}\delta p_{m,I}. \tag{69}$$

Then, we can follow the same procedure of the poroelastic porosity function (Equation 61) and its correction (Equation 62), by simply replacing K_{dr} with K_{dr}^{ep}, which yields

$$\Phi_l^{n+1} - \Phi_l^n = \left(\frac{\alpha_l^2}{K_l^{ep}} + \frac{\alpha_l - \Phi_l^n}{K_s}\right)\sum_{J=1}^{\mathrm{n}_p} S_{l,J}^{n+1}\left(p_{l,J}^{n+1} - p_{l,J}^n\right) - \Delta\Phi_c^l, \tag{70}$$

$$\Delta\Phi_c^l = \frac{b_l}{\eta_l}\underbrace{K_{dr}^{ep}\left\{\left(\varepsilon_v^n - \varepsilon_v^{n-1}\right) + \sum_{k=1}^{\mathrm{n}_m}\sum_{J=1}^{\mathrm{n}_p} b_{k,J}^n\left(p_{k,J}^n - p_{k,J}^{n-1}\right)\right\}}_{\left(\sigma_v^n - \sigma_v^{n-1}\right)}, \tag{71}$$

where n_p is the number of fluid phases.

6.3. *Well-posedness and admissibility of the constitutive relations*

The constitutive relations proposed in this study are desired to satisfy well-posedness just as those in single porosity systems because thermoporomechanics is dissipative physically and thus well-posed mathematical statements are required. We analyze the contractivity properties for the given mathematical problems and constitutive relations to investigate well-posedness. The analysis of contractivity was employed in the previous study of [37] for the single porosity model in order to determine a proper definition of pore-pressure for multiphase flow (i.e., an upscaled pressure from fluid phase pressures) between the equivalent and average pore-pressures, and it is found that the equivalent pore-pressure honors well-posedness, while the average pore-pressure, widely used in many engineering fields, does not.

Following the procedure of [37], in this section, we first evaluate admissibility of relations between local and global variables (i.e., Equations 45, 46, 52 – 55) and constitutive relations shown in Equations 63 – 66. Then, in the next section, we investigate whether the fixed-stress sequential scheme modified for multiple porosity systems is still contractive and numerically stable.

Let us introduce a norm extended from the single porosity model in [37] to the multiple porosity model, as follows.

$$\|\boldsymbol{\chi}\|_{\mathcal{H}}^2 = \frac{1}{2}\int\left(\sum_{l=1}^{\mathrm{n}_m}\eta_l\frac{K_l^{ep}}{K_{dr}^{ep}}\left(\boldsymbol{\varepsilon}_l^e : \mathbf{C}_l\boldsymbol{\varepsilon}_l^e + \boldsymbol{\xi}_l\cdot\mathbf{H}_l\boldsymbol{\xi}_l\right) + \left(\boldsymbol{\zeta}_e - \boldsymbol{b}^*\varepsilon_{v,e}\right)\cdot\mathbf{L}\left(\boldsymbol{\zeta}_e - \boldsymbol{b}^*\varepsilon_{v,e}\right)\right)d\Omega, \tag{72}$$

$$\begin{aligned}\mathcal{H} = \{\boldsymbol{\chi} :&= \left(\boldsymbol{\varepsilon}_1^e, \cdots, \boldsymbol{\varepsilon}_{\mathrm{n}_m}^e, \boldsymbol{\xi}_1, \cdots, \boldsymbol{\xi}_{\mathrm{n}_m}, \boldsymbol{\zeta}_e\right) \in \overbrace{\mathrm{S}\cdots\mathrm{S}}^{\mathrm{n_m}} \times \overbrace{\mathrm{R}^{\mathrm{n_{int}}}\cdots\mathrm{R}^{\mathrm{n_{int}}}}^{\mathrm{n_m}} \times \mathrm{R}^{\mathrm{n_p}\times\mathrm{n_m}} \\ &: \varepsilon_{l,ij}^e \in L^2(\Omega), \xi_{l,i} \in L^2(\Omega), \zeta_{(l,J)_e} \in L^2(\Omega)\},\end{aligned} \tag{73}$$

where $\mathrm{S} = \mathrm{R}^{(\mathrm{n_{dim}}+1)\times \mathrm{n_{dim}}/2}$, and $\mathrm{n_{dim}}$ and n_{int} are the dimension of the domain and the number of components of $\boldsymbol{\xi}_l$, respectively. $\boldsymbol{\varepsilon}_l^e = \left\{\varepsilon_{l,ij}^e\right\}$, $\boldsymbol{\xi}_l = \{\xi_{l,i}\}$, and $\boldsymbol{\zeta}_e = \left\{\zeta_{(l,J)_e}\right\}$, $\boldsymbol{b}^* = \left\{b_{l,J}^*\right\}$. Note that $\boldsymbol{\zeta}_e$ contains the number of materials of sub-elements.

Let us introduce two arbitrary initial conditions, $(\mathbf{u}_0,\ \mathbf{p}_0,\ \boldsymbol{\xi}_{l0})$ and $(\tilde{\mathbf{u}}_0,\ \tilde{\mathbf{p}}_0,\ \tilde{\boldsymbol{\xi}}_{l0})$, respectively, where $\mathbf{p} = \{p_{l,J}\}$. We also let $(\mathbf{u},\ \mathbf{p},\ \boldsymbol{\xi}_l)$ and $(\tilde{\mathbf{u}},\ \tilde{\mathbf{p}},\ \tilde{\boldsymbol{\xi}}_l)$ be the corresponding solutions from the two different initial conditions, which yield $(\boldsymbol{\varepsilon}_l^e,\ \boldsymbol{\zeta}_e,\ \boldsymbol{\kappa}_l)$ and $(\tilde{\boldsymbol{\varepsilon}}_l^e,\ \tilde{\boldsymbol{\zeta}}_e,\ \tilde{\boldsymbol{\kappa}}_l)$. The difference between the two solutions is denoted by $d(\cdot) = (\cdot) - \tilde{(\cdot)}$. Then, contractivity is defined as [1, 46, 47, 48, 49]

$$\frac{d}{dt}\left\|d\boldsymbol{\chi}\right\|_{\mathcal{H}} \leq 0. \tag{74}$$

Let the corresponding solutions from two arbitrary initial conditions be close enough, such that they follow the incremental forms of the constitutive relations and relations between local and global variables. Specifically, 'δ' in the relations such as Equations 45, 46, 54, 55, and 63 –66 can be replaced by 'd'.

Considering that the solutions from two arbitrary initial conditions satisfy the governing equations and the boundary conditions, the governing equations for multiphase flow and geomechanics yield

$$\mathrm{Div}\, d\boldsymbol{\sigma} = \mathbf{0},\ \ d\dot{m}_{l,J} + \mathrm{Div}\, d\boldsymbol{w}_{l,J} = 0, \tag{75}$$

where non-negative plastic dissipation is satisfied for elasto-plasticity, and homogeneous boundary conditions are obtained.

Then, the given mathematical problems based on the proposed constitutive relations yield contractivity, as follows.

$$\begin{aligned}
\frac{d}{dt}\left\|d\boldsymbol{\chi}\right\|_{\mathcal{H}}^2 &= \int\left(\sum_{l=1}^{n_m}\eta_l\frac{K_l^{ep}}{K_{dr}^{ep}}\left(\underbrace{d\boldsymbol{\varepsilon}_l^e:\mathbf{C}_l}_{=d\boldsymbol{\sigma'}_l}:d\dot{\boldsymbol{\varepsilon}}_l^e+\underbrace{d\boldsymbol{\xi}_l\cdot\mathbf{H}_l}_{=d\boldsymbol{\kappa}_l}d\dot{\boldsymbol{\xi}}_l\right)+\underbrace{(d\boldsymbol{\zeta}_e-\boldsymbol{b}^*d\varepsilon_{v,e})}_{=d\boldsymbol{\zeta}-\boldsymbol{b}^*d\varepsilon_v}\cdot\mathbf{L}\left(d\dot{\boldsymbol{\zeta}}_e-\boldsymbol{b}^*d\dot{\varepsilon}_{v,e}\right)\right)d\Omega,\\
&\qquad \text{(from Equations 45, 65, and 66 for } d\boldsymbol{\sigma'}_l,\ d\boldsymbol{\kappa}_l,\ \text{and } d\boldsymbol{\zeta}-\boldsymbol{b}^*d\varepsilon_v,\ \text{respectively)}\\
&= \int\left(\sum_{l=1}^{n_m}\eta_l d\boldsymbol{\sigma'}_l:\underbrace{\frac{K_l^{ep}}{K_{dr}^{ep}}d\dot{\boldsymbol{\varepsilon}}_l}_{=d\dot{\boldsymbol{\varepsilon}}}+\underbrace{(d\boldsymbol{\zeta}-\boldsymbol{b}^*d\varepsilon_v)\cdot\mathbf{L}}_{=d\mathbf{p}}(d\dot{\boldsymbol{\zeta}}-\boldsymbol{b}^*d\dot{\varepsilon}_v)\right)d\Omega\\
&\quad -\underbrace{\int\left(\sum_{l=1}^{n_m}\eta_l\frac{K_l^{ep}}{K_{dr}^{ep}}\left(d\boldsymbol{\sigma'}_l:d\dot{\boldsymbol{\varepsilon}}_l^p+d\boldsymbol{\kappa}_l\cdot d\dot{\boldsymbol{\xi}}_l\right)\right)d\Omega}_{\text{denoted by } D_p^d},\\
&\qquad \text{(from Equations 54 and 64 for } d\dot{\boldsymbol{\varepsilon}} \text{ and } dp_{l,J},\ \text{respectively)}\\
&= \int\left(\underbrace{d\boldsymbol{\sigma'}}_{=\sum_{l=1}^{n_m}\eta_l d\boldsymbol{\sigma'}_l}:d\dot{\boldsymbol{\varepsilon}}+d\mathbf{p}\cdot(d\dot{\boldsymbol{\zeta}}-\boldsymbol{b}^*d\dot{\varepsilon}_v)\right)d\Omega-D_p^d,\ \ \text{(from Equation 45 for } d\boldsymbol{\sigma'}),\\
&= \underbrace{\int d\boldsymbol{\sigma}:d\dot{\boldsymbol{\varepsilon}}d\Omega}_{=0}+\int d\mathbf{p}\cdot d\dot{\boldsymbol{\zeta}}d\Omega-D_p^d,\ \ \text{(from Equations 63 and } 75_1)\\
&= -\int d\boldsymbol{v}_{l,J}\cdot\boldsymbol{k}_{p,lJmI}^{-1}d\boldsymbol{v}_{m,J}d\Omega-D_p^d\leq 0,\quad v_{(l,J)_i}\in H\left(\mathrm{div},\Omega\right),
\end{aligned} \tag{76}$$

where the Darcy law (i.e., Equation 2) and divergence theorem are applied to the last expression, and non-negative plastic dissipation leads to $D_p^d \leq 0$. Thus, Equation 76 implies that the proposed constitutive relations (i.e., Equations 63 – 67), and globalization and localization (i.e., Equations 45, 46, 52 – 55) are admissible, honoring the dissipative mechanism in thermoporomechanics.

6.4. An a-priori stability estimate of the sequential scheme

Sequential schemes are typically limited by numerical stability and convergence. In particular, typical (obvious) sequential methods in coupled flow and geomechanics do not provide unconditional stability and the numerical instability cannot be fixed by reducing time step size [43]. Additionally, the typical methods may suffer from non-convergence, even in the case that they are numerically stable [32, 33]. According to [33], the fixed stress split method can provide unconditional stability and convergence with high accuracy for coupled flow and geomechanics in single porosity systems. In this section, for completeness, we will find that the fixed stress split modified for the multiple porosity model is still B-stable. As an a-priori estimate in numerical stability, we employ B-stability [1, 46, 47, 48, 49, 50], defined as

$$\left\| d\chi^{n+1} \right\|_{\mathcal{H}} \leq \left\| d\chi^{n} \right\|_{\mathcal{H}}, \tag{77}$$

where the corresponding mathematical statements satisfy contractivity. Following the definition of B-stability, we first investigate contractivity of the fixed-stress operator splitting modified for the multiple porosity model.

When the flow step is taken, the mathematical statements for multiphase flow are written as

$$d\dot{m}_{l,J} + \mathrm{Div}\, d\boldsymbol{w}_{l,J} = 0,\ \delta d\dot{\sigma} = 0,\ \mathrm{Div}\, d\dot{\sigma}_{t=0} = 0,\ \mathrm{Div}\, d\sigma_{t=0} = 0, \tag{78}$$

where homogeneous boundary conditions and non-negative plastic dissipation are satisfied. Same as the previous studies of single porosity systems [33], $\delta d\dot{\sigma} = 0$ with the initial conditions of Equation 78 yields

$$\mathrm{Div}\, d\sigma = 0. \tag{79}$$

Then, at the flow step, we obtain

$$\begin{aligned} \frac{d}{dt} \left\| d\boldsymbol{\chi} \right\|_{\mathcal{H}}^2 &= \underbrace{\int d\boldsymbol{\sigma} : d\dot{\boldsymbol{\varepsilon}} d\Omega}_{=0} + \int d\mathbf{p} \cdot d\dot{\boldsymbol{\zeta}} d\Omega - D_p^d,\ \text{(From Equation 79)}, \\ &= -\int d\boldsymbol{v}_{l,J} \cdot \boldsymbol{k}_{p,lJmI}^{-1} d\boldsymbol{v}_{m,J} d\Omega - D_p^d \leq 0. \end{aligned} \tag{80}$$

When we take the mechanics step, the mathematical statements are written as

$$\mathrm{Div}\, d\sigma = 0,\ dp_{l,J} = 0, \Rightarrow \mathrm{Div}\, d\sigma' = 0, \tag{81}$$

where non-negative plastic dissipation and homogeneous boundary conditions are satisfied. Then, we obtain

$$\begin{aligned} \frac{d}{dt} \left\| d\boldsymbol{\chi} \right\|_{\mathcal{H}}^2 &= \underbrace{\int d\boldsymbol{\sigma}' : d\dot{\boldsymbol{\varepsilon}} d\Omega}_{=0} - D_p^d,\ \text{(From Equation 81)}, \\ &= -D_p^d \leq 0. \end{aligned} \tag{82}$$

From Equations 80 and 82, the fixed-stress operator splitting holds contractivity. Since the operator splitting is contractive, we study the algorithmic numerical stability at the discrete time level (i.e., B-stability).

Consider the generalized midpoint rule in time discretization (evaluation at time t_β with $\beta \in (0, 1]$). We also consider typical return mapping algorithms for elastoplasticity for the associated

flow rule (maximum plastic dissipation) [45], which satisfies for material l within a gridblock

$$\underbrace{\ll \Sigma_l^{tr,n+\beta} - \Sigma_l^{n+\beta},\ \Pi_l - \Sigma_l^{n+\beta} \gg}_{\text{denoted by } D_l^A} \leq 0 \quad {}^{\forall}\Pi_l \in \mathcal{E}_l, \tag{83}$$

where the bilinear form $\ll \cdot, \cdot \gg$ is defined as

$$\ll \mathbf{\Sigma}_l, \mathbf{\Pi}_l \gg := \int_\Omega \left(\boldsymbol{\sigma}_l' : \mathbf{C}_l^{-1} \boldsymbol{\psi}_l' + \boldsymbol{\kappa}_l \cdot \boldsymbol{H}_l^{-1} \boldsymbol{\omega_l} \right) d\Omega, \tag{84}$$

and its associated norm $\| \cdot \|_{\mathcal{E}_l}$ is

$$\|\mathbf{\Sigma}_l\|_{\mathcal{E}_l}^2 := \frac{1}{2} \ll \mathbf{\Sigma}_l, \mathbf{\Sigma}_l \gg, \tag{85}$$

where $\mathbf{\Sigma}_l = (\boldsymbol{\sigma}_l', \boldsymbol{\kappa}_l)$ is a generalized effective-stress constrained to lie within the elastic domain $\mathcal{E}_l$, and $\mathbf{\Pi}_l = (\boldsymbol{\psi}_l', \boldsymbol{\omega}_l)$ is another (arbitrary) generalized effective stress. $\mathbf{\Sigma}_l^{tr,n+\beta}$ from the elastic trial step is defined as $(\boldsymbol{\sigma}_l'^n + \beta \mathbf{C}_l \Delta \boldsymbol{\varepsilon}_l^n, \boldsymbol{\kappa}_l^n)$.

Introducing the corresponding solutions, $\mathbf{\Sigma}$ and $\tilde{\mathbf{\Sigma}}$, from two arbitrary initial conditions and letting those be close enough, Equation 83 yields [32, 47]

$$\underbrace{\ll d\Sigma_l^n - d\Sigma_l^{n+\beta},\ -d\Sigma_l^{n+\beta} \gg + \ll (\beta \mathbf{C}_l \Delta d\varepsilon_l^n, 0),\ (-d\boldsymbol{\sigma}'^{n+\beta}_l, -d\boldsymbol{\kappa}_l^{n+\beta}) \gg}_{=D_l^A} \leq 0, \tag{86}$$

where the first term can identically be expressed as

$$\ll d\Sigma_l^n - d\Sigma_l^{n+\beta},\ -d\Sigma_l^{n+\beta} \gg = \beta \left(\left\| d\Sigma_l^{n+1} \right\|_{\mathcal{E}_l}^2 - \|d\Sigma_l^n\|_{\mathcal{E}_l}^2 \right) + \beta \left(2\beta - 1\right) \left\| d\Sigma_l^{n+1} - d\Sigma_l^n \right\|_{\mathcal{E}_l}^2. \tag{87}$$

The second term of Equation 87 yields

$$\begin{aligned}
&\sum_{l=1}^{\mathrm{n}_m} \eta_l \frac{K_l^{ep}}{K_{dr}^{ep}} \ll (\beta \mathbf{C}_l \Delta d\varepsilon_l^n, 0),\ (-d\boldsymbol{\sigma}'^{n+\beta}_l, -d\boldsymbol{\kappa}_l^{n+\beta}) \gg \\
&= -\beta \int \sum_{l=1}^{\mathrm{n}_m} \eta_l \underbrace{\frac{K_l^{ep}}{K_{dr}^{ep}} \Delta d\varepsilon_l^n}_{\Delta d\varepsilon^n} : d\boldsymbol{\sigma}'^{n+\beta}_l d\Omega = -\beta \int \underbrace{\sum_{l=1}^{\mathrm{n}_m} \eta_l d\boldsymbol{\sigma}'^{n+\beta}_l}_{d\boldsymbol{\sigma}'^{n+\beta}} : \Delta d\varepsilon^n d\Omega \\
&= -\beta \int \Delta d\varepsilon^n : (d\boldsymbol{\sigma}^{n+\beta} + b_{l,J}^* dp_{l,J}^{n+\beta} \mathbf{1}) d\Omega,
\end{aligned} \tag{88}$$

where Equation 63 is applied to the last expression. Then, from Equations 87 and 88, we obtain

$$\begin{aligned}
\sum_{l=1}^{\mathrm{n}_m} \eta_l \frac{K_l^{ep}}{K_{dr}^{ep}} \left(\left\| d\Sigma_l^{n+1} \right\|_{\mathcal{E}_l}^2 - \|d\Sigma_l^n\|_{\mathcal{E}_l}^2 \right) &= \sum_{l=1}^{\mathrm{n}_m} \eta_l \frac{K_l^{ep}}{K_{dr}^{ep}} \left(\frac{1}{\beta} D_l^A - (2\beta - 1) \left\| d\Sigma_l^{n+1} - d\Sigma_l^n \right\|_{\mathcal{E}_l}^2 \right) \\
&+ \int \Delta d\varepsilon^n : (d\boldsymbol{\sigma}^{n+\beta} + b_{l,J}^* dp_{l,J}^{n+\beta} \mathbf{1}) d\Omega.
\end{aligned} \tag{89}$$

When we solve the flow problem first, the algorithmic counterpart of Equation 78 at the discrete time level is written as

$$L_{lJmI}^{-1} (dp_{m,I}^{n+1} - dp_{m,I}^n) + b_{l,J}^* \overbrace{(d\varepsilon_v^{n+1} - d\varepsilon_v^n)}^{\Delta d\varepsilon_v^n} + \frac{\Delta t}{\rho_J} \operatorname{Div}(d\boldsymbol{w}_{l,J}^{n+\beta}) = 0, \tag{90}$$

$$d\boldsymbol{\sigma}^{n+1} - d\boldsymbol{\sigma}^n = d\boldsymbol{\sigma}^n - d\boldsymbol{\sigma}^{n-1},\ \operatorname{Div}\left(d\boldsymbol{\sigma}^1 - d\boldsymbol{\sigma}^0\right) = 0,\ \operatorname{Div} d\boldsymbol{\sigma}^0 = 0, \tag{91}$$

where we consider maximum plastic dissipation in the flow step because we use the elastoplastic moduli.

From Equation 91, we obtain

$$\mathrm{Div}\, d\boldsymbol{\sigma}^{n+\beta} = 0, \Rightarrow \int d\boldsymbol{\sigma}^{n+\beta} : \Delta d\boldsymbol{\varepsilon}^n d\Omega = 0. \tag{92}$$

Let us define a norm for $\mathbf{p}$ as

$$\|\mathbf{p}\|_{\mathcal{L}}^2 = \frac{1}{2}\int p_{l,J} L_{lJmI}^{-1} p_{m,I} d\Omega. \tag{93}$$

Consider the following identity

$$(\left\|d\mathbf{p}^{n+1}\right\|_{\mathcal{L}}^2 - \|d\mathbf{p}^n\|_{\mathcal{L}}^2) = \int_\Omega dp_{l,J}^{n+\alpha} L_{lJmI}\left(dp_{m,I}^{n+1} - dp_{m,I}^n\right) d\Omega - (2\beta-1)\left\|d\mathbf{p}^{n+1} - d\mathbf{p}^n\right\|_{\mathcal{L}}^2. \tag{94}$$

Then, at the flow step, adding Equations 89 and 94 with Equations 90 and 92, the evolution of the norm is described as

$$\begin{aligned}
\left\|d\chi^{n+1}\right\|_{\mathcal{H}}^2 - \|d\chi^n\|_{\mathcal{H}}^2 &= \sum_{l=1}^{\mathrm{n}_m} \eta_l \frac{K_l^{ep}}{K_{dr}^{ep}}\left(\left\|\boldsymbol{\Sigma}^{n+1}\right\|_{\mathcal{E}_l}^2 - \|\boldsymbol{\Sigma}^n\|_{\mathcal{E}_l}^2\right) + \left(\left\|\mathbf{p}^{n+1}\right\|_{\mathcal{L}}^2 - \left\|\mathbf{p}^{n+1}\right\|_{\mathcal{L}}^2\right) \\
&= \sum_{l=1}^{\mathrm{n}_m} \eta_l \frac{K_l^{ep}}{K_{dr}^{ep}}\left(\frac{1}{\beta}\underbrace{D_l^A}_{\leq 0} - (2\beta-1)\left\|d\Sigma_l^{n+1} - d\Sigma_l^n\right\|_{\mathcal{E}_l}^2\right) + \underbrace{\int \Delta d\varepsilon^n : d\boldsymbol{\sigma}^{n+\beta} d\Omega}_{=0} \\
&\quad - (2\beta-1)\left\|d\mathbf{p}^{n+1} - d\mathbf{p}^n\right\|_{\mathcal{L}}^2 - \int \frac{\Delta t}{\rho_J}\mathrm{Div}(d\boldsymbol{w}_{l,J}^{n+\beta}) d\Omega \\
&\leq -(2\beta-1)\sum_{l=1}^{\mathrm{n}_m} \eta_l \frac{K_l^{ep}}{K_{dr}^{ep}}\left\|d\Sigma_l^{n+1} - d\Sigma_l^n\right\|_{\mathcal{E}_l}^2 - (2\beta-1)\left\|d\mathbf{p}^{n+1} - d\mathbf{p}^n\right\|_{\mathcal{L}}^2 \\
&\quad - \Delta t \int d\boldsymbol{v}_{l,J}^{n+\beta} \cdot \boldsymbol{k}_{p,lJmI}^{-1} d\boldsymbol{v}_{m,J}^{n+\beta} d\Omega,
\end{aligned} \tag{95}$$

from which B-stability is obtained at the flow step when $\beta \geq 0.5$.

When we solve the mechanics problem at the next step, the algorithmic counterpart of Equation 81 at the discrete time level is written as

$$\mathrm{Div}\, d\sigma^{n+\beta} = 0,\ dp_{l,J}{}^{n+\beta} = 0, \Rightarrow \mathrm{Div}\, d\sigma'^{n+\beta} = 0, \tag{96}$$

where the maximum plastic dissipation is satisfied. Then, at the mechanics step, adding Equations 89 and 94 with Equation 96, we obtain the evolution of the norm as

$$\begin{aligned}
\left\|d\chi^{n+1}\right\|_{\mathcal{H}}^2 - \|d\chi^n\|_{\mathcal{H}}^2 &= \sum_{l=1}^{\mathrm{n}_m} \eta_l \frac{K_l^{ep}}{K_{dr}^{ep}}\left(\frac{1}{\beta}\underbrace{D_l^A}_{\leq 0} - (2\beta-1)\left\|d\Sigma_l^{n+1} - d\Sigma_l^n\right\|_{\mathcal{E}_l}^2\right) \\
&\quad + \underbrace{\int \Delta d\varepsilon^n : (d\boldsymbol{\sigma}'^{n+\beta}) d\Omega}_{=0} - (2\beta-1)\left\|d\mathbf{p}^{n+1} - d\mathbf{p}^n\right\|_{\mathcal{L}}^2,
\end{aligned} \tag{97}$$

from which B-stability is obtained at the mechanics step when $\beta \geq 0.5$. Thus, from Equatins 95 and 97, the fixed-stress sequential method modified for multiple porosity systems are unconditionally stable when $\beta \geq 0.5$.

Equation 83 implies that the return mapping is performed for all materials of sub-elements. In solution procedure, after we obtain the global total strain, we calculate the local total stain from Equation 54_3, followed by the return mapping, which determines local plastic variables, hardening moduli, and elastoplastic tangent moduli. Then, we can determine global properties such as global elastic and plastic strains from Equations 54 and 55. Since return mapping is performed at each sub-element, we can employ different plastic models, yield conditions, and hardening laws for different materials.

6.5. Porosity correction in thermoporoelasticity

Let us incorporate Equations 19 and 33 into the following equation for thermoporomechanics:

$$\begin{pmatrix} \delta\varepsilon_v \\ \delta\zeta \\ \delta\mathbf{\Lambda} \end{pmatrix} = \begin{pmatrix} a & -\mathbf{b}^T & -\tilde{\mathbf{b}}^T \\ -\mathbf{b} & \mathbf{L}^{-1} & -\bar{\mathbf{D}} \\ -\tilde{\mathbf{b}} & -\bar{\mathbf{D}} & \tilde{\mathbf{D}} \end{pmatrix} \begin{pmatrix} \delta\sigma_v \\ \delta\mathbf{p} \\ \delta\mathbf{T} \end{pmatrix}, \tag{98}$$

$$\mathbf{\Lambda} = \begin{pmatrix} \bar{S}_1 - \bar{s}_{1,J}\delta m_J \\ \vdots \\ \bar{S}_{\mathrm{n}_m} - \bar{s}_{\mathrm{n}_m,J}\delta m_J \end{pmatrix}, \bar{\mathbf{D}} = \begin{pmatrix} \bar{d}_{1\,1} & \cdots & \bar{d}_{1\,\mathrm{n}_m\times\mathrm{n}_p} \\ \vdots & \ddots & \vdots \\ \bar{d}_{\mathrm{n}_m\times\mathrm{n}_p\,1} & \cdots & \bar{d}_{\mathrm{n}_m\times\mathrm{n}_p\,\mathrm{n}_m\times\mathrm{n}_p} \end{pmatrix}, \tag{99}$$

where $\bar{\mathbf{D}}$ is determined by coupling beween fluid flow and heat transfer, regardless of geomechanics. The off-diagonal terms of $\bar{\mathbf{D}}$ are typically zero, just as $\mathbf{D}$ and $\tilde{\mathbf{D}}$. The diagonal terms of $\bar{\mathbf{D}}$ are determined by $3\alpha_T^l\alpha_{l,J} - 3\alpha_{m,J}^l$ for material l and phase J. Then, we can determine all the coefficients in Equation 98 from the results obtained previously in poromechanics and thermomechanics.

For numerical simulation in non-isothermal condition, we can extend the fixed-stress split method straightforwardly, when employing one-way coupling from heat flow to mechanics. This one-way coupling implies that a direct contribution from mechanics to heat flow is neglected (i.e., $\tilde{\mathbf{b}} = \mathbf{0}$ of the third row of Equation 98). The one-way coupling can be justified when a heat capacity of material or fluid is high, or direct heat generation from deformations is negligible [22]. However, mechanics can still affect heat flow coupled to fluid flow because fluid flow and mechanics are tightly (two-way) coupled. Then, based on one-way coupling from heat flow to mechanics and the fixed-stress split method, at the flow step where fluid and heat flow problems are solved simultaneously for flow, the porosity function and its correction for the non-isothermal condition become

$$\Phi_l^{n+1} - \Phi_l^n = \left(\frac{\alpha_l^2}{K_l} + \frac{\alpha_l - \Phi_l^n}{K_s}\right)\sum_{J=1}^{\mathrm{n}_p} S_J^{n+1}\left(p_{l,J}^{n+1} - p_{l,J}^n\right) + 3\alpha_{T,l}\alpha_l\left(T_l^{n+1} - T_l^n\right) - \Delta\Phi_c^l, \tag{100}$$

$$\Delta\Phi_c^l = \frac{b_l}{\eta_l}\underbrace{K_{dr}\left\{\left(\varepsilon_v^n - \varepsilon_v^{n-1}\right) + \sum_{k=1}^{\mathrm{n}_m}\sum_{J=1}^{\mathrm{n}_p} b_{k,J}\left(p_{k,J}^n - p_{k,J}^{n-1}\right) + \sum_{k=1}^{\mathrm{n}_m}\tilde{b}_k\left(T_k^n - T_k^{n-1}\right)\right\}}_{\left(\sigma_v^n - \sigma_v^{n-1}\right)}. \tag{101}$$

From the mathematical standpoint, one-way coupling from heat flow to mechanics implies decoupling between heat flow and mechanics, so we infer that the a priori stability estimate shown previously for isothermal condition can still validate the unconditional stability of the fixed-stress split for this non-isothermal condition. However, finding sequential methods that hold B-stability when $\tilde{\mathbf{b}}$ in the third row of Equation 98 is not neglected is an open question, which cannot be encompassed by the a priori stability estimate in this study.

7. NUMERICAL EXAMPLES

We introduce three cases for testing poroelasticity, poroelastoplasticity, and thermoporoelasticity in multiple porosity systems. We use fracture-rock matrix systems for the multiple porosity systems. The fracture-rock matrix systems are representative of any composite systems that consist of a high permeable material transporting fluid over the domain and the other materials storing fluid and conveying it to the high permeable material, as shown in Figure 3. Thus, the fracture medium in these numerical examples does not need to be a physical fracture, but represents a high permeable material.

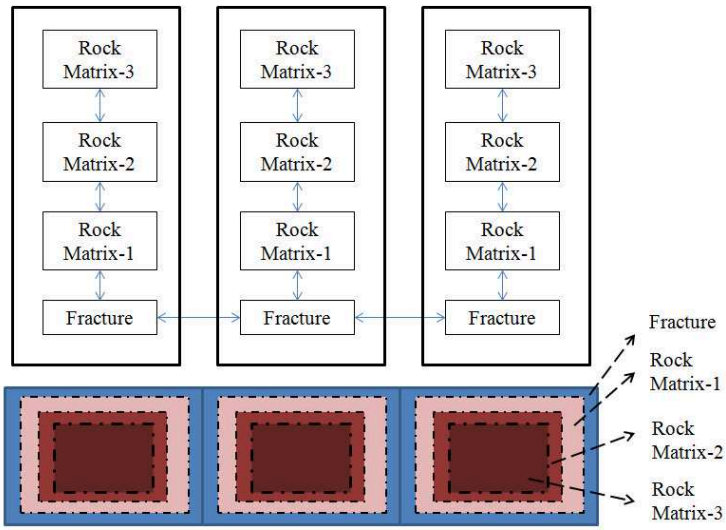

Figure 3. A representative fracture-rock matrix system (i.e., MINC) is described [28]. Fluid flows through the fractures, while the rock matrices provide fluid into the fracture continuum. The arrow, ↔, implies fluid flow.

7.1. Poroelasticity

We introduce a 1D consolidation problem for single phase fluid flow and isothermal condition, using the MINC method for flow. The domain has 9 gridblock, where the grid spacing Δx, Δy, and Δz are 1 m, 1 m, and 2 m, respectively. Each gridblock has five interacting continua (i.e., 5 sub-elements): one fracture and four rock matrix media, as shown in Figure 4. Accordingly, the flow problem has 45 elements, while the mechanical problem has 9 elements. Volume fractions of Fracture, Matrices 1, 2, 3 and 4 are 0.02, 0.08, 0.2, 0.35, and 0.35, respectively. An observation gridblock is located at the bottom.

For flow, the initial permeability and porosity of the fracture continuum are $k_p^{f,0} = 598\ md$, where $1\ md = 9.87 \times 10^{-16}\ m^2$, and $\phi_{f,0} = 0.5$, while those for each rock matrix continuum are $k_p^{m,0} = 0.0598\ md$ and $\phi_{m,0} = 0.3$. We assume constant permeability during simulation, focusing on interactions between mechanical deformation and fluid pressure for the proposed constitutive relations of multiple porosity systems, although appropriate permeability models for dynamic permeability would be necessary for real simulation. There is no gravity. The fluid (water) compressibility is $c_w = 4.7 \times 10^{-10}\ Pa^{-1}$. The fluid density and viscosity are $\rho_w = 1000$ kg m^{-1} and $\mu_w = 1.0$ cp (1.0 cp $= 10^{-3} Pa \cdot s$). We have a no-flow boundary at the bottom and a drainage boundary on the top, at which the boundary fluid pressure is $P_{bc} = 10\ MPa$. Initial fluid pressure is $P_i = 10\ MPa$.

For mechanics, linear elasticity is considered. The global (upscaled) drained bulk modulus is $K_{dr} = 300\ MPa$ and the shear modulus is $G = 450\ MPa$, from which Poisson's ratio is $\nu = 0.0$. We consider different drained bulk moduli for numerical tests of different porosity systems. We

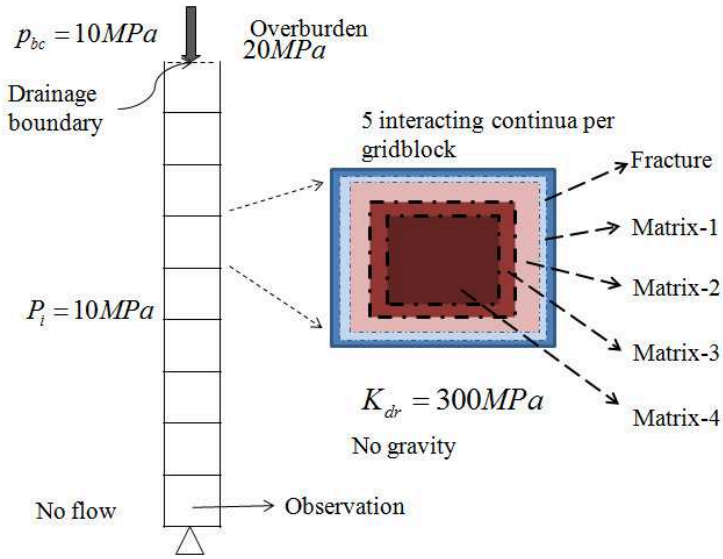

Figure 4. 1D consolidation problem with five interacting continua in flow. We test three porosity systems in mechanics: single, double, and five porosity systems. All the porosity systems yield the same upscaled drained bulk modulus for mechanics (i.e., $K_{dr} = 300\ MPa$).

have no displacement at the bottom, horizontally constrained boundary conditions at sides, and the overburden, $\bar{\sigma} = 20\ MPa$ on top. Initial total stress is $\sigma_0 = 10\ MPa$. Note that this consolidation problem is a modification from Terzaghi's problem, where the fluid pressure rises instantaneously at $t = 0$ due to the instant loading effect, and then decreases due to the drainage of the fluid from the domain to the top boundary.

We consider the single, double, and five porosity systems. For the single porosity system, we assign a single drained bulk modulus $300\ MPa$ to the five continua. For the double porosity system, the drained bulk moduli of Fracture K_f and Matrix 1 K_{M_1} are $31.25\ MPa$, while those of Matrices 2, 3, and 4 (i.e., K_{M_2} , K_{M_3}, and K_{M_4}) are $6.75\ GPa$. For the five porosity system, we have $K_f = 7.125\ MPa$, $K_{M_1} = 154.1\ MPa$, $K_{M_2} = 30\ GPa$, $K_{M_3} = 675\ GPa$, and $K_{M_4} = 2363\ GPa$. Poisson's ratios for all materials for all porosity systems are 0.0. We assign the five different drained bulk moduli to represent a wide range for high heterogeneity within a gridblock as well as to achieve clear differences from the single and double porosity systems. Note that all the porosity systems yield the same global drained bulk modulus of the gridblock, $K_{dr} = 300\ MPa$. This implies that the three different porosity systems can exhibit same apparent geomechanical properties when physical experiments at the gridblock level (i.e., macroscopic view) are conducted, even though there are different degrees of heterogeneity within a given gridblock (i.e., microscopic view).

From the left of Figure 5, the single porosity system shows the same instantaneous pressure buildup between fracture and rock matrix media because the two bulk moduli are the same. Then, the (fluid) pressure in Fracture decreases rapidly because of high permeability, while the pressure in Matrix 1 also decreases, but slowly because of low permeability.

On the other hand, the double porosity system shows different instantaneous pressure buildup between (Fracture, Matrix 1) and (Matrices 2, 3 and 4) because the two bulk moduli are different (the right of Figure 5). Then the pressure in Fracture decreases at a slower rate than that of the single porosity system because the bulk modulus of Fracture in the double porosity system is lower than that of the single porosity system.

Interestingly, after the instantaneous pressure buildup at $t = 0$, the pressures in all Matrices drop at early time (1) because the decrease of the pressure in Fracture causes compression of Fracture, accompanied by dilation of Matrices to balance the overall deformation of the gridblock, and (2)

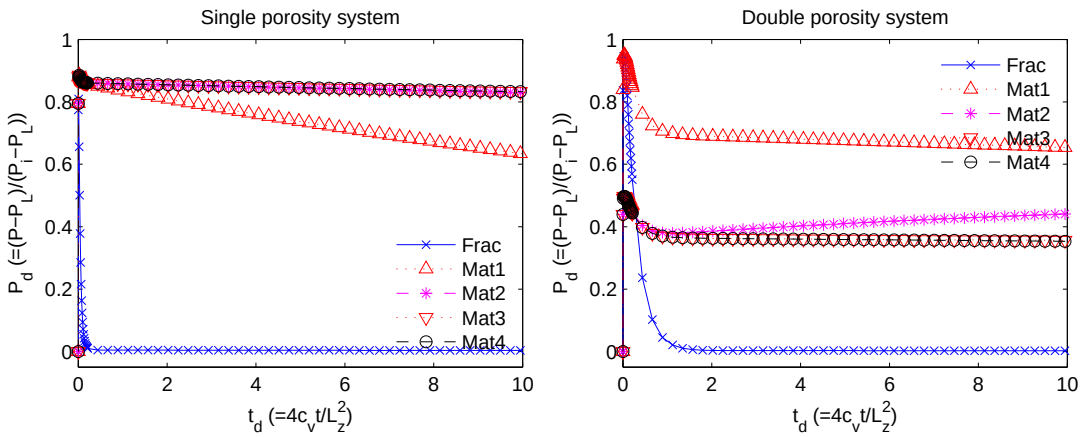

Figure 5. Results from the single (left) and double (right) porosity models. P_d and t_d are the dimensionless pressure and time in the 1D problem, where $P_d = \frac{P-P_L}{P_i-P_L}$ and $t_d = \frac{4c_v t}{(L_z)^2}$. P_L is the lower limit of the pressure during simulation. Here, $P_L = P_{bc}$. c_v is the consolidation coefficient defined as $c_v = \frac{k_p^{f,0}}{(1/K_{dr}+\phi_{m,0}c_w)\mu_w}$. L_z is the vertical length of the reservoir domain. When using the single porosity model, we cannot distinguish deformation of the fracture medium from those of the rock matrix medium properly, showing the same pressure buildup. However, the double porosity model can capture the distinct deformation of the fracture medium, showing different pressure buildups. 'Frac', 'Mat1', 'Mat2', 'Mat3', and 'Mat4' indicate Fracture, Matrices 1, 2, 3, and 4, respectively.

because the fluid flows into Fracture. After the pressure in Fracture is in equilibrium, reaching the boundary pressure, the pressure in Matrix 1 decreases, but very slowly because of low permeability.

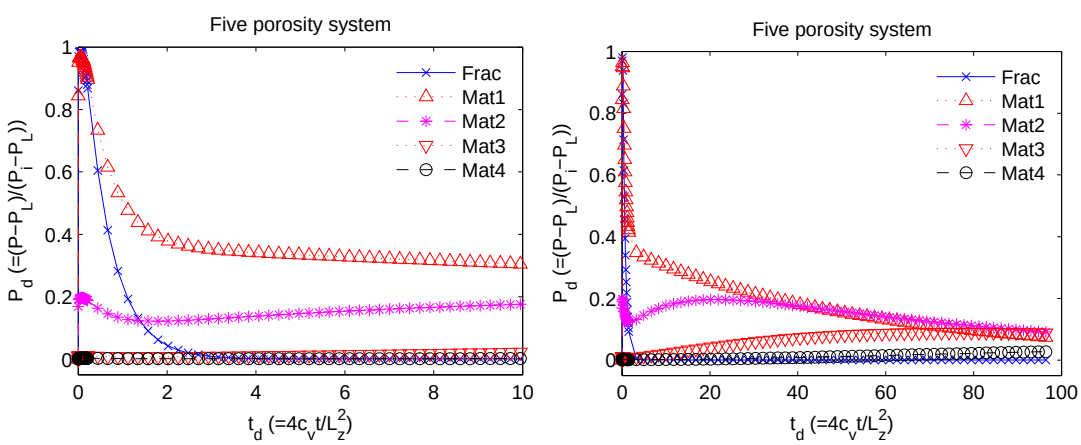

Figure 6. Results from the five porosity model for $t_d = 10$ (left) and $t_d = 100$ (right). The five different bulk modulus system represents more complicated behavior in fluid pressure than the single and double porosity systems because it can reflect high heterogeneity within a gridblock.

In the five porosity system, all materials have different instantaneous pressure buildups, as shown in Figure 6. As the drained bulk moduli of the materials are lower, the corresponding pressure buildups become higher. After the instantaneous pressure buildup in Fracture, the pressure in Fracture decreases due to the drainage boundary on the top. Compared to single and double porosity systems, the pressure drop in Fracture in this five porosity system is relatively slow, because a low drained bulk modulus yields high total compressibility of the flow problem, mitigating pressure diffusion. In Matrix 1, at initial time, fluid pressure decreases fast due to dilation of Matrices and flow into Fracture, same as the double porosity system. After the pressure in Fracture becomes

constant, the pressure in Matrix 1 drops slowly. Matrix 2 shows that, at initial time, the pressure decreases fast due to compression of Fracture. Then, the pressure increases due to influx of fluid from Matrix 1. As the difference in fluid pressure between Matrices 1 and 2 decreases, the rate of the pressure increase becomes slow. Eventually, the pressure in Matrix 2 decreases due to outflux into Fracture through Matrix 1. Matrices 3 and 4 have the same behavior as Matrix 2. Only differences are some degrees of the pressure value and time scale. Compared with the results for the double porosity system, the five porosity system can realize more various patterns in pressure, reflecting high heterogeneity within a gridblock.

7.2. Poroelastoplasticity

We investigate elastoplastic behavior in the multiple porosity systems, employing the Mohr-Coulomb model [51, 52], which is widely used to model failure of cohesive frictional materials. The yield criterion f and the plastic potential function g are written as

$$f = \tau'_m - \sigma'_m \sin\Psi_f - c_h \cos\Psi_f \leq 0, \tag{102}$$

$$g = \tau'_m - \sigma'_m \sin\Psi_d - c_h \cos\Psi_d \leq 0, \tag{103}$$

$$\sigma'_m = \frac{\sigma'_1 + \sigma'_3}{2} \quad \text{and} \quad \tau'_m = \frac{\sigma'_1 - \sigma'_3}{2}, \tag{104}$$

where c_h Ψ_f and Ψ_d are the cohesion, friction and dilation angles, respectively. σ'_1, σ'_2, and σ'_3 are the maximum, intermediate, and minimum principal effective stresses, respectively.

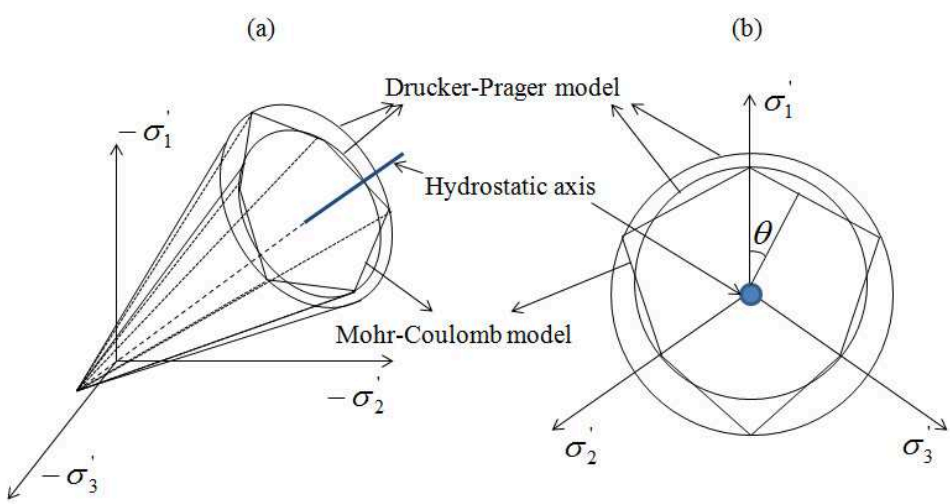

Figure 7. The yield surfaces of the Mohr-Coulomb and Drucker-Prager models on (a) the principle effective stress space and (b) on the deviatoric plane. All the effective stresses are located inside the yield surfaces.

As shown in Figure 7, the yield function of the Mohr-Coulomb model includes six corners and a common vertex on the tension side of the hydrostatic axis. The discontinuous corners may cause numerical instability in return mapping [52, 53]. In order to handle the discontinuity problem in the return mapping of the Mohr-Coulomb model, we adopt the Drucker-Prager model around the discontinuous corners, as employed by [52], which is written as

$$f = \beta_f I_1 + \sqrt{J_2} - k_f \leq 0, \tag{105}$$

$$g = \beta_g I_1 + \sqrt{J_2} - k_g \leq 0, \tag{106}$$

where β_f, k_f, β_g, and k_g are given as

$$\beta_f = \frac{\sin \Psi_f}{0.5\left(3(1-\sin\Psi_f)\sin\theta + \sqrt{3}(3+\sin\Psi_f)\cos\theta\right)}, \tag{107}$$

$$k_f = \frac{3c_h}{0.5\left(3(1-\sin\Psi_f)\sin\theta + \sqrt{3}(3+\sin\Psi_f)\cos\theta\right)}, \tag{108}$$

$$\beta_g = \frac{\sin \Psi_d}{0.5\left(3(1-\sin\Psi_d)\sin\theta + \sqrt{3}(3+\sin\Psi_d)\cos\theta\right)}, \tag{109}$$

$$k_g = \frac{3c_h}{0.5\left(3(1-\sin\Psi_d)\sin\theta + \sqrt{3}(3+\sin\Psi_d)\cos\theta\right)}, \tag{110}$$

where θ is the Lode angle [51, 52], written as

$$\theta = \frac{1}{3}\cos^{-1}\left(\frac{3\sqrt{3}}{2}\frac{J_3}{J_2^{3/2}}\right). \tag{111}$$

I_1, J_2, and J_3 are invariants of the effective stresses as follows

$$I_1 = \mathrm{tr}\boldsymbol{\sigma'}, \quad J_2 = \frac{1}{2}\boldsymbol{s'}:\boldsymbol{s'}, \quad J_3 = \det\boldsymbol{s'}, \quad \text{where} \quad \boldsymbol{s'} = \boldsymbol{\sigma'} - \frac{I_1}{3}\mathbf{1}. \tag{112}$$

The Drucker-Prager model has the smooth and continuous surface at $\theta = 0, \pi/3$, while the Mohr-Coulomb model shows the discontinuity at the two points. We employ the return mapping algorithm proposed by [52] for the Mohr-Coulomb plasticity simulation.

We reuse the previous one dimensional problem of the five porosity system, using the same fluid and geomechanical properties. For the Mohr-Coulomb model, we have $\Psi_f = 0$ and $\Psi_d = 0$ for both Fracture and Matrices. We use a wide range of the cohesion values in the five materials for high heterogeneity within a gridblock, as shown in Table I. Note that Fracture represents a weak and high permeable porous medium, which does not need to be a physically fractured medium.

Table I. Cohesion for Fracture and Matrices

Cohesion	Fracture	Matrix 1	Matrix 2	Matrix 3	Matrix 4
c_h	$2.8\ MPa$	$280\ MPa$	$28\ GPa$	$2800\ GPa$	$2800\ GPa$

Figure 8 shows that pressures in Fracture and Matrices are higher when elastoplasticity is considered than when only elastic mechanics is employed. At initial time, Fracture faces failure because of low cohesion, while Matrices are still elastic because of high cohesion. This failure of Fracture can change the mechanical properties and variables for the mechanical problem such as elastoplastic tangent moduli and total strain. As a result, changes in mechanics yield more compaction not only in Fracture but also in all Matrices, leading to higher pressures than those in elasticity, as shown in Figure 8.

Figures 9 (a) and (b) show vertical and horizontal plastic strains in Fracture and gridblock at the observation gridblock. Even though we have relatively large local plastic strains at Fracture, the

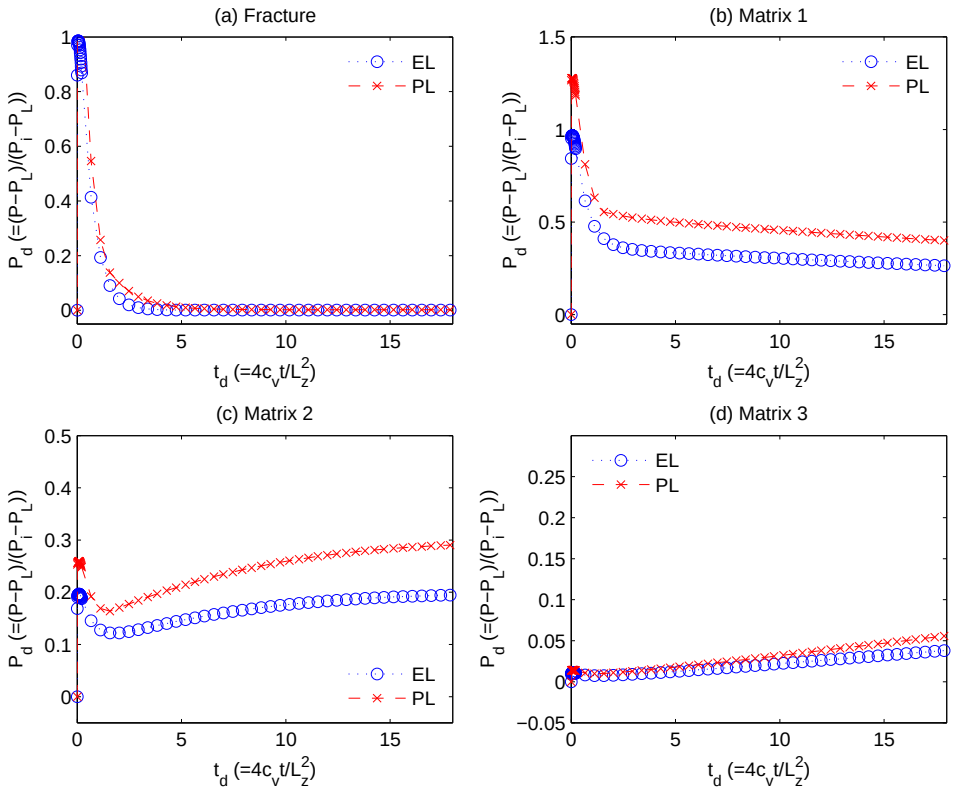

Figure 8. Results of the five porosity model in elasticity and elastoplasticity. 'EL' and 'PL' denote elasticity and elastoplasticity. Pressures in Fracture and Matrices in elastoplasticity are higher than those in elasticity because Fracture enters the plastic regime, yielding larger compaction. The compaction can support the reservoir pressure.

global (upscaled) plastic strains (i.e., gridblock strain) are still small, because Matrices are elastic. This can validate the assumption of infinitesimal transformation in mechanics. From Figures 9 (c) and (d), Fracture enters elasticity after initial plasticity. Then, we reenter the plastic region. Since we have $\Psi_d = 0.0$, $\varepsilon_{v,p} = 0.0$ is obtained. Material failure occurs on the edge of the Mohr-Coulomb yield surface, $\theta = 0$, so the return mapping based on the Drucker-Prager model is used when Fracture experiences plasticity. Note that, in this numerical example, we obtain $\sqrt{J_2} = 3.151\ MPa$ at Fracture in plasticity, which matches the analytical solution of the Drucker-Prager model.

7.3. Thermoporoelasticity

We use a non-isothermal plane strain two dimensional (2D) problem to investigate thermoporomechanics in multiple porosity systems. The 2D domain is divided into 20×10 uniformly-sized gridblocks in (x, z) with $\Delta x = 10\ m$, $\Delta y = 10\ m$, and $\Delta z = 10\ m$, as shown in Figure **??**. Each gridblock has five porous materials: one fracture and four rock matrices. Volume fractions of Fracture, Matrices 1, 2, 3 and 4 are 0.02, 0.08, 0.2, 0.35, and 0.35, respectively.

For flow, the fluid compressibility is $c_f = 4.7 \times 10^{-10}\ Pa^{-1}$. The fluid density and viscosity are $\rho_w = 1000$ kg m^{-1} and $\mu_w = 1.0$ cp. We have no-flow boundary conditions at all boundaries. Initial fluid pressure and temperature are $P_i = 19\ MPa$ and $T_i = 146.7^oC$. The initial porosity of Fracture is $\phi_{f,0} = 0.5$, while that for each Matrix is $\phi_{m,0} = 0.3$. The initial permeability of Fracture is $k_p^{f,0} = 598\ md$. We have a specific heat capacity of $1000\ J\ kg^{-1}\ ^oC$ for both Fracture and Matrices, and use the specific heat capacity of water for given pressure and temperature conditions. Fluid is produced from Fracture in Well 2 of the gridblock located at (row, column) = (5, 1) at a

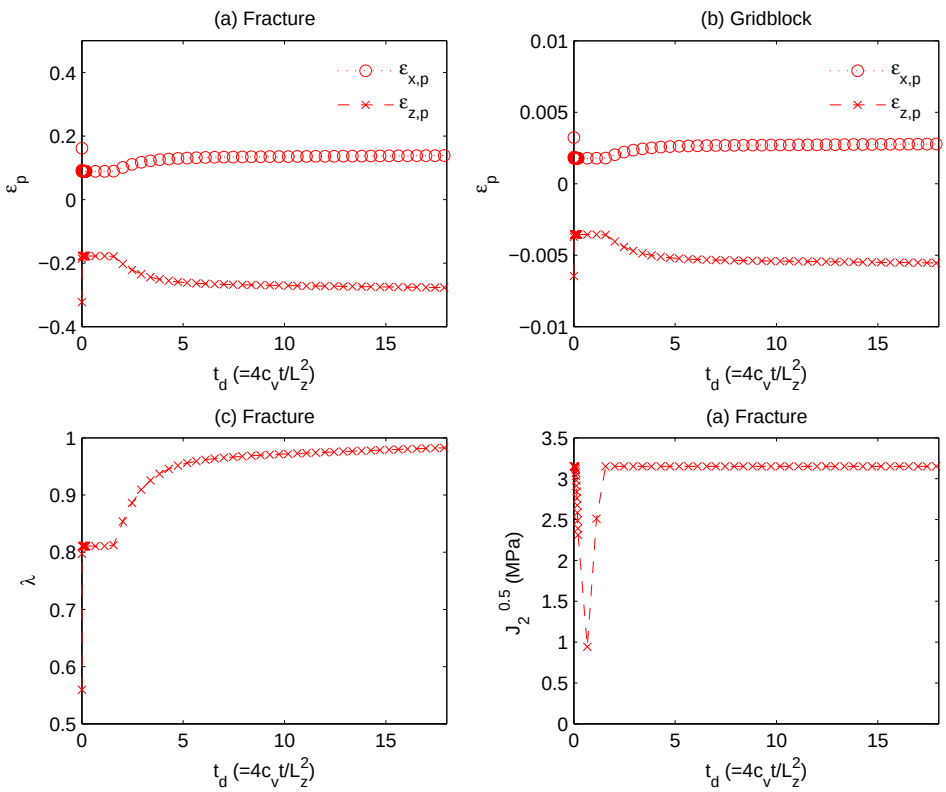

Figure 9. Evolution of the plastic strains in (a) Fracture and (b) gridblock, (c) plastic multiplier λ, also called plastic consistency parameter, at Fracture, and (d) $\sqrt{J_2}$ at Fracture. $\varepsilon_{z,p}$ and $\varepsilon_{x,p}$ denote vertical and horizontal plastic strains, respectively. The low cohesion of Fracture causes initial failure, while Matrices are still elastic.

total mass rate of $Q_p = 10\ kg/s$, while liquid water at 20^oC is injected to Fracture in Well 1 of the gridblock located at (row, column) = (5, 15) at a total mass rate of $Q_{inj} = 10\ kg/s$.

The permeability is $k_p = 49.35 \times 10^{-15}\ m^2$, 50 md,

heat conductivity is $k_T =$ thermal dilation coefficients α_T

The permeability is constant during simulation, and there is no gravity.

For mechanics, linear elasticity is considered. Young's modulus is $E = 100\ MPa$, and Poisson's ratio is $\nu = 0.0$. We have a no-displacement boundary at the bottom, horizontally constrained boundary conditions at sides, and the overburden, $\bar{\sigma} = 19\ MPa$ on the top boundary. Then, we have initial principal total stresses of $-19\ MPa$, resulting in no strain changes at $t = 0$. Biot's coefficient is $b = 1.0$, which yields $K_s = \infty$.

In this section, we study differences between thermoporomechanics and the uncoupled conventional reservoir simulation that employs a rock (pore) compressibility. We choose the rock compressibility that can provide results closest to those of the thermoporoelastic simulation. In this 2D case, the 3D drained bulk modulus is used for rock compressibility in the uncoupled reservoir simulation, not the constrained modulus.

Case 3.1: $\alpha_T = 0\ ^oC^{-1}$, $k_T = 0\ Wm^{-1}\ ^oC^{-1}$, *and* $k_p^m = 0\ md$ We first consider the case where the Matrix permeability k_p^m as well as heat conductivity k_T and thermal dilation coefficients α_T of Fracture and Matrices are zero. Thus, fluid/heat flow occurs only in Fracture, and coupling between heat transfer and geomechanics is not considered.

Figure 10 shows that liquid water pressure increases within Fracture at Well 1 (Figure 10 (a)) because liquid water is injected into Fracture. The increase of pressure in Fracture results in dilation

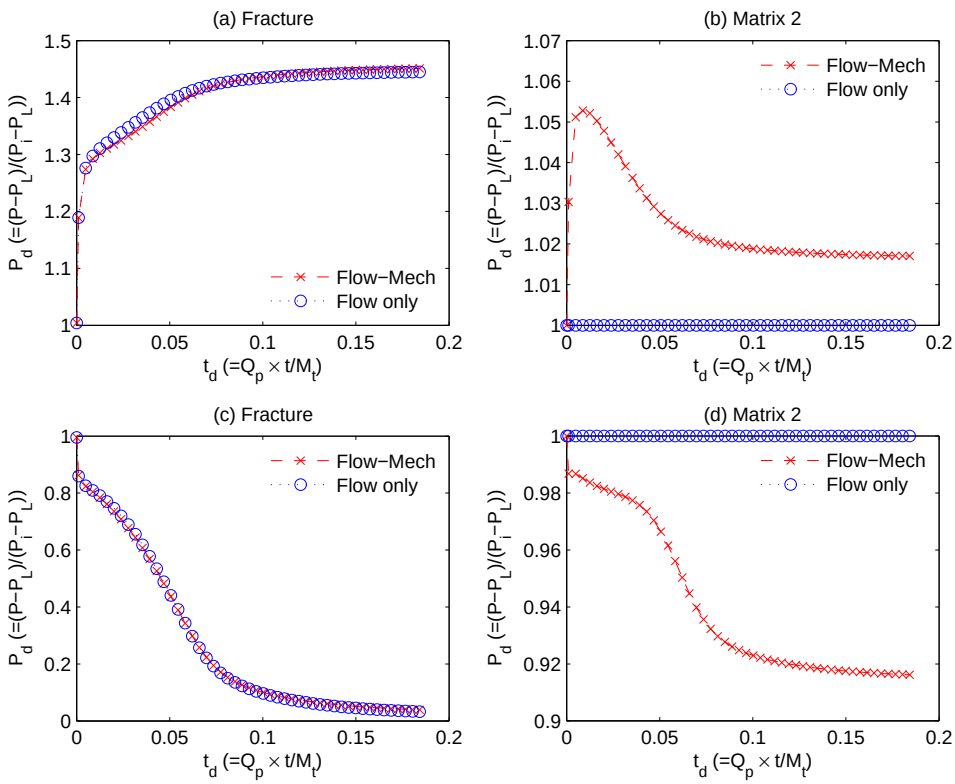

Figure 10. Evolution of pressure at the monitoring wells for Case 3.1: (a) pressure in Fracture at the injection well (Well 1), (b) pressure in Matrix 2 at the injection well (Well 1), (c) pressure in Fracture at the production well (Well 2), (d) pressure in Matrix 2 at the production well (Well 2). $P_d = \frac{P-P_L}{P_i-P_L}$ and $t_d = Q_p \times t/M_i$, where $P_L = 16\ MPa$ and M_i is the initial reservoir fluid mass-in-place. We observe variations of the pressure in Matrix 2 when employing the coupled simulation, capturing the effects from mechanics of Fracture (i.e., compaction/dilation of Fracture).

of Fracture, which can cause compaction of Matrices to balance overall deformation of the gridblock (Figure 10 (b)). Then, the compaction of Matrices can induce the increase of the pressure in Matrices. At the production well (Well 2), the pressure in Fracture decreases because of water production (Figure 10 (c)), which leads to compaction of Fracture. As opposed to the injection well, Matrices expand and cause the pressure drop (Figure 10 (d)).

In contrast with the coupled simulation, the uncoupled reservoir simulation with the rock compressibility cannot capture changes in pressure in Matrices at Wells 1 and 2. Figure 11 shows that we observe no difference in temperature between the coupled and conventional reservoir simulations, because there is no heat flow between Fracture and Matrix 1 as well as between Matrices due to zero heat conductivity and no thermal coupling from/to geomechanics.

Case 3.2: $\alpha_T = 7.5 \times 10^{-4}\ {}^oC^{-1}$, $k_T = 0\ Wm^{-1}\ {}^oC^{-1}$, *and* $k_p^m = 0\ md$ We use a high thermal dilation coefficient $\alpha_T = 7.5 \times 10^{-4}\ {}^oC^{-1}$ with the previous test case, and examine differences between the coupled and uncoupled reservoir simulations, investigating thermal effects in mechanics and fluid/heat flow. We choose the thermal expansivity of the flow-only simulation that can provide results closest to those of thermporoelastic simulation, same as the determination of rock compressibility.

We observe higher increase of pressure in Fracture at the injection well $P_d = 1.9$ (21.7 MPa) than the previous case $P_d = 1.5$ (20.35 MPa), as shown in Figure 12 (a). Cold water injection induces thermal compaction within Fracture, which contributes to larger buildup of pressure. In

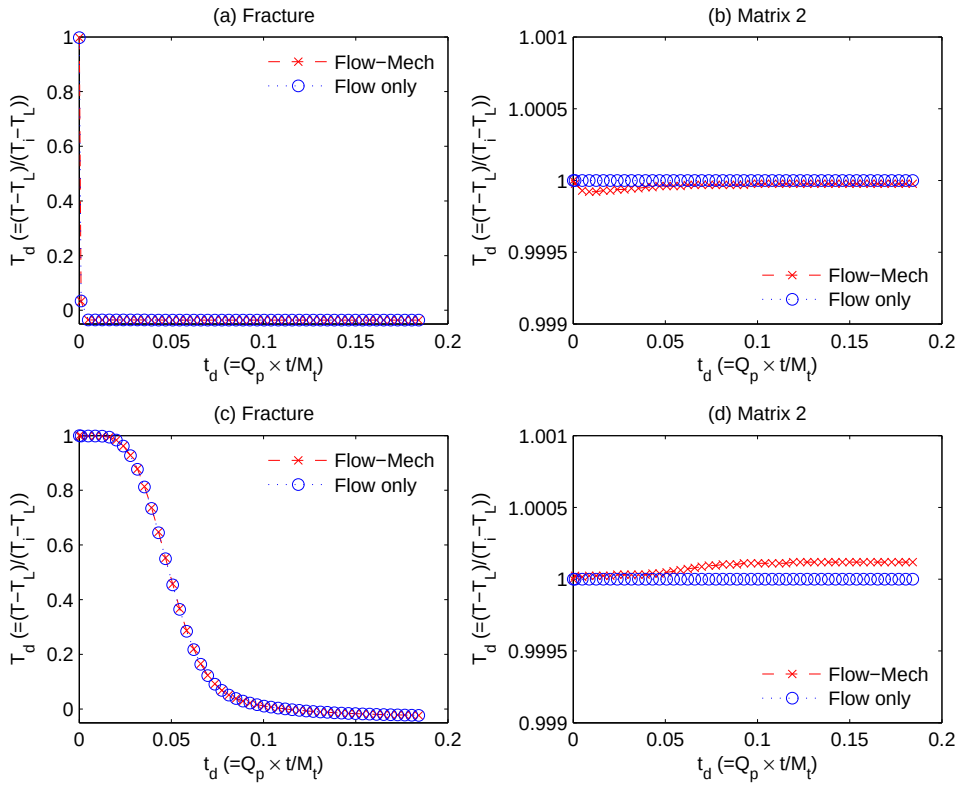

Figure 11. Evolution of temperature at the monitoring wells for Case 3.1: (a) temperature in Fracture at the injection well, (b) temperature in Matrix 2 at the injection well, (c) temperature in Fracture at the production well, (d) temperature in Matrix 2 at the production well. $T_d = \frac{T-T_L}{T_i-T_L}$ is dimensionless temperature. In this test case, $T_L = 20^oC$. We obtain the same temperature between the coupled and uncoupled simulations because of no thermal coupling and zero heat conductivity.

Fracture, compaction by the cooling prevails against dilation induced by fluid mass injection in this test case. Compaction of Fracture induces dilation of Matrices. As a result, the pressures in Matrices at Well 1 (injection well) drop below the initial pressure (Figure 12 (b)).

At the production well, the pressure in Fracture drops almost instantaneously due to fluid production (Figure 12 (c)). After the pressure drop, as the pressure in Fracture at the injection well increases, the pressure in Fracture at the production well also increases because of pressure diffusion. When cold water enters the production well, compaction of Fracture can contribute to more pressure buildup. After the increase of the pressure in Fracture at early times, the pressure in Fracture deceases again because variations of the pressure in Fracture at the injection well and of the temperature in Fracture at the production well decrease eventually.

In Matrix 2 at the production well, we observe instantaneous pressure drop because of dilation of Matrix 2 caused by compaction of Fracture due to fluid production (Figure 12 (d)). Afterward, as the increase of the pressure in Fracture induces dilation of Fracture, compaction of Matrix 2 reduces the pressure drop at early times. Then, the pressure in Matrix 2 drops faster because compaction from the decrease of the pressure in Fracture induces dilation of Matrix 2. These complicated physical behaviors fundamentally result from close interactions between fluid/heat flow and geomechanics.

Note that Matrices are impermeable, so there is no pressure diffusion between the materials within a gridblock. Thus, changes in the pressure in Matrices result from the effects from the changes in geomechanics (i.e., coupled fluid/heat flow and geomechanics). On the other hands, the uncoupled reservoir simulation cannot capture these coupled phenomena, showing no change in the pressure in Matrices at both injection and production wells.

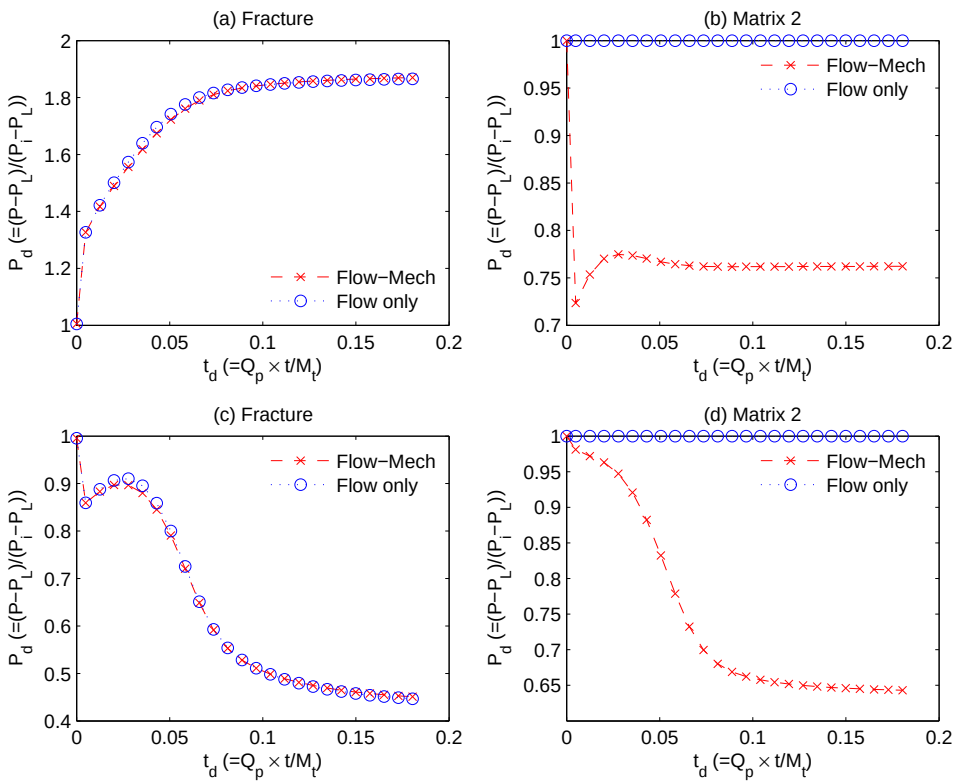

Figure 12. Evolution of pressure at the monitoring wells for Case 3.2: (a) pressure in Fracture at the injection well, (b) pressure in Matrix 2 at the injection well, (c) pressure in Fracture at the production well, (d) pressure in Matrix 2 at the production well. Due to coupled fluid/heat flow and geomechanics, we observe variations of the pressure in Matrix 2, even though the Matrix permeability is zero, while the uncoupled simulation cannot capture the variations.

Case 3.3: $\alpha_T = 7.5 \times 10^{-4}\ {}^oC^{-1}$, $k_T = 3.1\ Wm^{-1}\ {}^oC^{-1}$, *and* $k_p^m = 0.0598\ md$ In the third case, we employ high thermal conductivity and non-zero rock matrix permeability. We observe from Figure 13 that results from the coupled and uncoupled simulations have similar physical trends. However, although the uncoupled simulation shows the similarities to the coupled simulation, we still observe differences at late times, as shown in Figure 13. Thus, coupled flow and geomechanics need to be considered for accuracy when flow and geomechanics are tightly coupled for the cases of highly deformable or stress-sensitive reservoirs.

8. CONCLUSIONS

We have generalized constitutive relations of poroelasticity for the double porosity model to those for the multiple porosity model, determining coupling coefficients between fluid flow and geomechanics. Especially, in the case of zero values in the off-diagonal terms of the total compressibility matrix for isothermal condition in fluid flow, which is typically employed in reservoir simulation, the upscaled drained bulk modulus for mechanics becomes a volume-fraction weighted harmonic average of drained bulk moduli of the materials of sub-elements. For the given coupling coefficients, we also determined the upscaled elastic moduli. Then, we immediately extended the coefficients and constraints of poroelasticity to thermoelasticity and poroelastoplasticity. Specifically, for poroelastoplasticity, elastoplastic tangent moduli instead of elastic moduli are used for the coupling coefficients. We also showed that the constitutive equations and relations between local and global variables proposed in this study hold well-posedness,

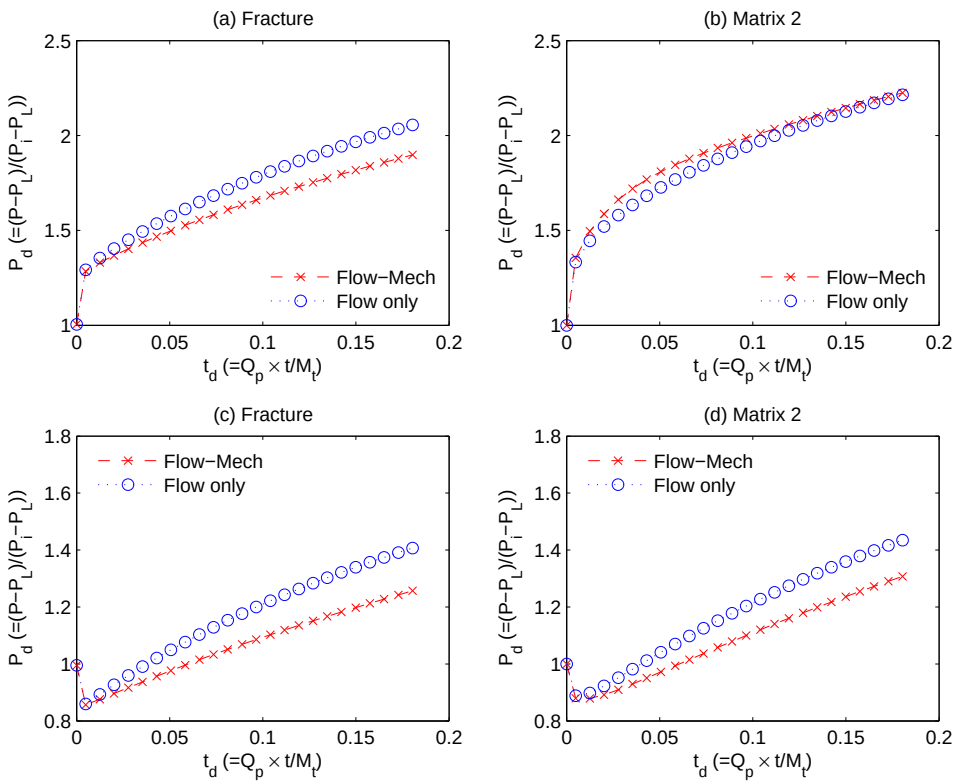

Figure 13. Evolution of pressure at the monitoring wells for Case 3.3: (a) pressure in Fracture at the injection well, (b) pressure in Matrix 2 at the injection well, (c) pressure in Fracture at the production well, (d) pressure in Matrix 2 at the production well. We find differences between the coupled and uncoupled simulations to become larger as the simulations proceed.

implying that the proposed relations are admissible in the sense of the physically dissipative mechanism of thermoporomechanics.

To solve these extremely complicated coupled problems, we employed the fixed-stress sequential method modified for the multiple porosity model and showed by the energy method that the sequential method provides unconditional stability. This sequential method can easily be implemented in reservoir simulation by using the Lagrange porosity function and its correction modified for the multiple porosity model. We provided formulations for the porosity functions and corrections for poroelasticity, poroelastoplasticity, and thermoporomechanics with single or multi-phase flow for the multiple porosity model. In the case of elastoplasticity, the return mapping is performed at each sub-element.

We tested three cases: poroelasticity, poroelastoplasticity, and thermoporoelasticity for single phase flow. In poroelasticity, single, double, and five porosity systems were used, and we found that the multiple porosity model can reflect the characteristics of high heterogeneity within a gridblock. For poroelastoplasticity, using the Mohr-Coulomb failure model, we detected the plastic behaviors of a weak material such as the fracture medium in the five porosity system, which could have not been captured if the single porosity model had been used. In thermoporoelasticity, the coupled simulation showed extremely complicated physics for the three sub-test cases, and we observed significant differences between the coupled and uncoupled simulations.

In conclusions, neglecting geomechanics in composite materials such as a fracture-rock matrix system may cause large errors, and considering geomechanical properties of composite materials can provide an accurate modeling for coupled flow and geomechanics, for example, in fractured porous media. The modeling and numerical algorithms for thermoporomechanics proposed in

this paper are considerably useful for mechanically or thermally sensitive regularly fractured or composite reservoirs, and readily applicable to large scale problems.

ACKNOWLEDGEMENTS

This work was supported by the American Recovery and Reinvestment Act (ARRA), through the Assistant Secretary for Energy Efficiency and Renewable Energy (EERE), Office of Technology Development, Geothermal Technologies Program, of the U.S. Department of Energy under Contract No. DE-AC02-05CH11231. We are grateful to the two anonymous reviewers for their constructive reviews.

REFERENCES

[1] Armero F, Simo JC. A new unconditionally stable fractional step method for non-linear coupled thermomechanical problems. *Int. J. Numer. Meth. Engrg.* 1992; **35**:737–766.

[2] Armero F, Simo JC. A prior stability estimates and unconditionally stable product formula algorithms for nonlinear coupled thermoplasticity. *Int. J. Plasticity* 1993; **9**:749–782.

[3] Rutqvist J, Stephansson O. The role of hydromechanical coupling in fractured rock engineering. *Hydrogeology Journal* 2003; **11**:7–40.

[4] Zienkiewicz OC, Paul DK, Chan AHC. Unconditionally stable staggered solution procedure for soil-pore fluid interaction problems. *Int. J. Numer. Meth. Engrg.* 1988; **26**(5):1039–1055.

[5] Coussy O, Eymard R, Lassabatére T. Constitutive modeling of unsaturated drying deformable materials. *J. Eng. Mech.* 1998; :658–557.

[6] Armero F. Formulation and finite element implementation of a multiplicative model of coupled poro-plasticity at finite strains under fully saturated conditions. *Comput. Methods Appl. Mech. Engrg.* 1999; **171**:205–241.

[7] Coussy O. Poromechanics of freezing materials. *J. Mech. Phys. Solids* 2005; :1689–1718.

[8] White AJ, Borja RI. Stabilized low-order finite elements for coupled solid-deformation/fluid-diffusion and their application to fault zone transients. *Comput. Methods Appl. Mech. Engrg.* 2008; **197**:43534366.

[9] Bagheri M, Settari A. Modeling of geomechanics in naturally fractured reservoirs. *SPE Reserv. Eval. Eng.* 2008; **11**(1):108–118.

[10] Merle HA, Kentie CJP, van Opstal GHC, Schneider GMG. The bachaquero study - a composite analysis of the behavior of a compaction drive/solution gas drive reservoir. *J. Pet. Technol.* Sep 1976; :1107–1114.

[11] Lewis RW, Sukirman Y. Finite element modelling of three-phase flow in deforming saturated oil reservoirs. *Int. J. Numer. Anal. Methods Geomech.* 1993; **17**:577–598.

[12] Kosloff D, Scott R, Scranton J. Finite element simulation of wilmington oil field subsidence: I. linear modelling. *Tectonophysics* 1980; **65**:339–368.

[13] Rutqvist J, Moridis GJ. Numerical studies on the geomechanical stability of hydrate-bearing sediments. *Soc. Pet. Eng. J.* 2009; **14**(2):267–282.

[14] Kim J, Moridis GJ, Yang D, Rutqvist J. Numerical studies on two-way coupled fluid flow and geomechanics in hydrate deposits. *Soc. Pet. Eng. J.* In press; SPE141304.

[15] Cappa F, Rutqvist J. Impact of co2 geological sequestration on the nucleation of earthquakes. *Geophys. Res. Lett.* 2011; **38**:L17 313.

[16] Rutqvist J, Barr D, Birkholzer JT, Fujisaki K, Kolditz O, Liu QS, Fujita T, Wang W, Zhang CY. A comparative simulation study of coupled thm processes and their effect on fractured rock permeability around nuclear waste repositories. *Environ. Geol.* 2009; **57**:1347–1360.

[17] Rutqvist J, Freifeld B, Min KB, Elsworth D, Tsang Y. Analysis of thermally induced changes in fractured rock permeability during eight years of heating and cooling at the yucca mountain drift scale test. *Int. J. Rock. Mech. Min. Sci.* 2008; **45**:1375–1389.

[18] Biot MA. General theory of three-dimensional consolidation. *J. Appl. Phys.* 1941; **12**:155–164.

[19] Geertsma J. The effect of fluid pressure decline on volumetric change of porous rocks. *Trans. AIME* 1957; **210**:331–340.

[20] Biot MA, Willis DG. The elastic coefficients of the theory of consolidation. *J. Appl. Phys.* 1957; :594–601.

[21] Coussy O. *Mechanics of porous continua*. John Wiley and Sons: Chichester, England, 1995.

[22] Lewis RW, Schrefler BA. *The finite element method in the static and dynamic deformation and consolidation of porous media*. Second edn., Wiley: Chichester, England, 1998.

[23] Settari A, Mourits F. A coupled reservoir and geomechanical simulation system. *Soc. Pet. Eng. J.* 1998; **3**:219–226.

[24] Borja RI. On the mechanical energy and effective stress in saturated and unsaturated porous continua. *Int. J. Solids Structures* 2006; **12**:1764–1786.

[25] Berryman JG, Wang HF. The elastic coefficients of double-porosity models for fluid transport in jointed rock. *J. Geophys. Res.* 1995; **100**:24,611 – 24,627.

[26] Bai M. On equivalence of dual-porosity poroelastic parameters. *J. Geophys. Res.* 1999; **104**:10,461 – 10,466.

[27] Berryman JG. Extension of poroelastic analysis to double-porosity materials: New technique in microgeomechanics. *J. Eng. Mech. ASCE* 2002; **128**(8):840 – 847.

[28] Pruess K, Narasimhan TN. A practical method for modeling fluid and heat flow in fractured porous media. *Soc. Pet. Eng. J.* 1985; **25**(1):14 – 26.

[29] Barenblatt GE, Zheltov IP, Kochina IN. Basic concepts in the theory of seepage of homogeneous liquids in fissured rocks. *J. Appl. Math.* 1960; **24**(5):1286 – 1303.

[30] Borja RI, Koligi A. On the effective stress in unsaturated porous continua with double porosity. *J. Mech. Phys. Solid* 2009; **57**:1182–1193.

[31] Taron J, Elsworth D, Min K. Numerical simulation of thermo-hydrologic-mechanical-chemical processes in deformable, fractured porous media. *Int. J. Rock Mech. Min.* 2009; **46**:842 – 854.

[32] Kim J, Tchelepi HA, Juanes R. Stability and convergence of sequential methods for coupled flow and geomechanics: Drained and undrained splits. *Comput. Methods Appl. Mech. Engrg.* 2011; **200**:2094–2116.

[33] Kim J, Tchelepi HA, Juanes R. Stability and convergence of sequential methods for coupled flow and geomechanics: Fixed-stress and fixed-strain splits. *Comput. Methods Appl. Mech. Engrg.* 2011; **200**:1591–1606.

[34] Lewis RW, Ghafouri HR. A novel finite element double porosity model for multiphase flow through deformable fractured porous media. *Int. J. Numer. Anal. Methods Geomech.* 1997; **21**:789 – 816.

[35] Masters I, Pao WKS, Lewis RW. Coupling temperature to a double-porosity model of deformable porous media. *Int. J. Numer. Meth. Engrg.* 2000; **49**:421–438.

[36] Aziz K, Settari A. *Petroleum Reservoir Simulation*. Elsevier: London, 1979.

[37] Kim J, Tchelepi HA, Juanes R. Rigorous coupling of geomechanics and multiphase flow with strong capillarity. *Soc. Pet. Eng. J.* In minor revision; SPE 141268.

[38] Moridis GJ, Kowalsky MB, Pruess K. Tough+hydrate v1.0 user's manual: A code for the simulation of system behavior in hydrate-bearing geologic media. *Report LBNL-00149E*, Lawrence Berkeley National Laboratory, Berkeley, CA, 2008.

[39] Xu T, Sonnenthal E, Spycher N, Pruess K. Toughreact user's guide: A simulation program for non-isothermal multiphase reactive geochemical transport in variably saturated geologic media. *LBNL-55460-2008*, Lawrence Berkeley National Laboratory, Berkeley, CA, 2008.

[40] Hughes TJR. *The Finite Element Method: Linear Static and Dynamic Finite Element Analysis*. Prentice-Hall: Englewood Cliffs, NJ, 1987.

[41] Jha B, Juanes R. A locally conservative finite element framework for the simulation of coupled flow and reservoir geomechanics. *Acta Geotechnica* 2007; **2**:139–153.

[42] Vermeer PA, Verruijt A. An accuracy condition for consolidation by finite elements. *Int. J. Numer. Anal. Methods Geomech.* 1981; **5**:1–14.

[43] Kim J, Tchelepi HA, Juanes R. Stability, accuracy, and efficiency of sequential methods for coupled flow and geomechanics. *Soc. Pet. Eng. J.* 2011; **16**(2):249–262. SPE-119084-PA.

[44] Coussy O. *Poromechanics*. John Wiley and Sons: Chichester, England, 2004.

[45] Simo JC, Hughes TJR. *Computational inelasticity*. Springer: Heidelberg, 1998.

[46] Hundsdorfer WH, Splijer ML. A note on b-stability of runge-kutta methods. *Numer. Math.* 1981; **36**:319–331.

[47] Simo J. Nonlinear stability of the time-discrete variational problem of evolution in nonlinear heat conduction, plasticity and viscoplasticity. *Comput. Methods Appl. Mech. Engrg.* 1991; **88**:111–131.

[48] Simo J, Govindjee S. Nonlinear b-stability and symmetry preserving return mapping algorithms for plasticity and viscoplasticity. *Comput. Methods Appl. Mech. Engrg.* 1991; **31**:151–176.

[49] Araújo A. A note on b-stability of splitting methods. *Comput. Visual. Sci.* 2004; **6**:53–57.

[50] Romero I. Thermodynamically consistent time-stepping algorithms for non-linear thermomechanical systems. *Int. J. Numer. Meth. Engrg.* 2009; **79**:706–732.

[51] Bathe K. *Finite element procedures*. Prentice-Hall: Englewood Cliffs, NJ, 1996.

[52] Wang X, Wang LB, Xu LM. Formulation of the return mapping algorithm for elastoplastic soil models. *Comput. Geotech.* 2004; **31**:315–338.

[53] Borja RI, Sama KM, Sanz PF. On the numerical integration of three-invariant elastoplastic constitutive models. *Comput. Methods Appl. Mech. Engrg.* 2003; **192**:1227–1258.

DISCLAIMER

This document was prepared as an account of work sponsored by the United States Government. While this document is believed to contain correct information, neither the United States Government nor any agency thereof, nor The Regents of the University of California, nor any of their employees, makes any warranty, express or implied, or assumes any legal responsibility for the accuracy, completeness, or usefulness of any information, apparatus, product, or process disclosed, or represents that its use would not infringe privately owned rights. Reference herein to any specific commercial product, process, or service by its trade name, trademark, manufacturer, or otherwise, does not necessarily constitute or imply its endorsement, recommendation, or favoring by the United States Government or any agency thereof, or The Regents of the University of California. The views and opinions of authors expressed herein do not necessarily state or reflect those of the United States Government or any agency thereof or The Regents of the University of California.

Ernest Orlando Lawrence Berkeley National Laboratory is an equal opportunity employer.